This is the peer reviewed author accepted manuscript (post print) version of a published work that appeared in final form in:

Dharmayanti, Cintya, Clulow, Andrew J, Gillam, Todd A, Klingler-Hoffmann, Manuela, Albrecht, Hugo, Blencowe, Anton 2024 'Position matters: pyridine regioisomers influence secondary structure and micelle morphology in polymer-homopolypeptide micelles', Biomacromolecules, online, pp. 1-15

This un-copyedited output may not exactly replicate the final published authoritative version for which the publisher owns copyright. It is not the copy of record. This output may be used for non-commercial purposes.

The final definitive published version (version of record) is available at:
https://doi.org/10.1021/acs.biomac.4c00204

Persistent link to the UniSA Research Outputs Repository:
https://researchoutputs.unisa.edu.au/11541.2/39174

General Rights

Copyright and moral rights for the publications made accessible in the UniSA Research Outputs Repository are retained by the authors and/or other copyright owners and it is a condition of accessing publications that users recognize and abide by the legal requirements associated with these rights.

- Users may download and print one copy for the purpose of private study or research.
- You may not further distribute the material or use it for any profit-making activity or commercial gain
- You may freely distribute the persistent link identifying the publication in the UniSA Research Outputs Repository

If you believe that this document breaches copyright, please contact us and provide details. We will remove access to the work immediately and investigate your claim.

Position matters: Pyridine regioisomers influence secondary structure and micelle morphology in polymer-homopolypeptide micelles

*Cintya Dharmayanti[1], Andrew J. Clulow[2], Todd A. Gillam[1], Manuela Klingler-Hoffmann[3], Hugo Albrecht[4], Anton Blencowe[1]**

[1] Applied Chemistry and Translational Biomaterials (ACTB) Group, Centre for Pharmaceutical Innovation, Clinical and Health Sciences, University of South Australia, Adelaide, SA 5001, Australia

[2] Australian Synchrotron, Australian Nuclear Science and Technology Organisation (ANSTO), Clayton, VIC 3168, Australia

[3] Clinical and Health Sciences, University of South Australia, Adelaide, SA 5001, Australia

[4] Centre for Pharmaceutical Innovation, Clinical and Health Sciences, University of South Australia, Adelaide, SA 5001, Australia

Abstract

Polymer-homopolypeptide block copolymers are a class of bioinspired materials that combine the processability and stability of synthetic polymers with the biocompatibility and unique secondary structures of peptides, such as α-helices and β-sheets. These properties make them ideal candidates for a wide variety of applications, for example in the pharmaceutical field, where they are frequently explored as building blocks for polymeric micelle drug delivery systems. While homopolypeptide side chains can be furnished with an array of different moieties to impart the copolymers with desirable properties, such as stimulus responsivity, pyridine derivatives represent an under-utilised functional group for this purpose. Additionally, the interplay between polypeptide side chain structure, secondary conformation, and micelle morphology is not yet well understood, particularly in the case of structural regioisomers. Therefore, in this work, a series of polymer-homopolypeptide copolymers were prepared from a poly(ethylene glycol)-*b*-poly(glutamic acid) (PEG-*b*-PGA) backbone, where the pendant carboxylic acid groups were covalently conjugated to a series of pyridine regioisomers by carbodiimide coupling. These pyridine regioisomers differed only in the position of the nitrogen heteroatom — *ortho, meta* or *para*, relative to the linking group — generating a series of PEG-*b*-poly(pyridinylmethyl glutamate) (PEG-*b*-PMG) copolymers. Following self-assembly of the copolymers in aqueous solutions, dynamic light scattering (DLS) revealed differences in micelle hydrodynamic diameter (D_h) (ranging from ~ 60–120 nm), while transmission electron microscopy (TEM) and small-angle X-ray scattering (SAXS) revealed distinctive morphologies ranging from ellipsoidal, to cylindrical, and disc-like, suggesting that subtle changes in positional isomers in the polypeptide block may influence the micelle structure. Analysis of the PEG-*b*-PMG copolymer micelles by circular dichroism (CD) and attenuated total reflectance Fourier transform infrared (ATR-FTIR) spectroscopy revealed that differences in the morphology were associated with changes in

polypeptide secondary structure, which in turn was influenced by the position of the pyridine heteroatom. Overall, these findings contribute to the broader understanding of the relationship between polypeptide structure and micelle morphology, and serve as useful insight for the rational design of polymer-polypeptide nanoparticles.

KEYWORDS: Copolymer; micelle; nanoparticle; morphology; polypeptide; regioisomer.

Introduction

Polymer-polypeptide block copolymers are bioinspired materials that contain both a synthetic polymer block and synthetic polypeptide block. They have been extensively used in the preparation of polymeric micelles for drug delivery applications due to their favourable biocompatibility, biodegradability, and ability to form unique secondary structures such as α-helices and β-sheets; a property that is virtually impossible to achieve with traditional synthetic polymers alone.[1, 2]

While many amphiphiles containing short peptides with specific primary sequences have been investigated for drug delivery applications,[3, 4] this work focuses on block copolymers containing repeating units of identical amino acids, otherwise known as polymer-homopolypeptides. These polymer-homopolypeptides are often prepared *via* ring opening polymerisation (ROP) of *N*-carboxyanhydrides (NCAs); an approach widely used due to its facile synthesis, scalability, high yield, and ability to generate polypeptides of defined molecular weight and specific tacticity.[5] Copolymers containing poly(glutamate)-based blocks, for example, have been widely explored as building blocks for cancer-targeted micelles,[6, 7] where they are reported to adopt α-helical conformations in solution.[8-10] α-Helices and β-sheets are spatially well-defined, and when incorporated into larger self-assemblies (e.g., micelles), can influence the resulting morphology of the nanoparticle.[2, 11, 12] Much of the existing literature in the area of polymer-homopolypeptides has focused on the effect of the degree of polymerisation (DP) or weight fraction of the polypeptide block (i.e., *f*) on the morphology of the nanoparticles. For instance, Grazon *et al.* prepared a series of poly(ethylene glycol)-*b*-poly(leucine) (PEG-*b*-PLeu) copolymers with different block lengths *via* aqueous ROP induced self-assembly to produce particles with rod-like morphologies.[13] PLeu blocks with higher DPs resulted in more pronounced β-sheet secondary

structures, which in turn controlled the dimensions of the cylindrical nanostructures and their anisotropy.[13] In addition, Chécot *et al.* prepared poly(butadiene)-*b*-PGA copolymers and found that they formed spherical micelles when the weight fraction of the PGA block (f_{PGA}) ≥ 0.85 and vesicles when the f_{PGA} = 0.74.[14]

While a significant amount of interesting work has been done to investigate the relationship between the molecular weight of the polypeptide and nanoparticle morphology, fewer studies have explored how this morphology is influenced by polypeptide side chain structure. In one notable example, Kramer *et al.* reported block copolypeptides with pendant galactopyranosyl groups conjugated through either alkylamide or alkylsulfone linkers, resulting in different secondary conformations and aggregate morphologies.[15] The copolypeptides with alkylamide linkers adopted rigid α-helical conformations in solution, while the addition of alkylsulfone linkers disrupted the α-helical conformation and generated disordered conformations. This, in turn, resulted in different nanostructures, whereby the copolypeptides with alkylsulfone linkers formed vesicles and those with alkylamide linkers formed irregular, micron sized aggregates. This was attributed to the rigidity of the α-helices, compacting these segments and preventing their ability to stabilise the assemblies from aggregation. Li *et al.* prepared poly(γ-benzyl-L-glutamate) (PBG) copolymers grafted with PEG at various grafting densities between 20–36% and found that the morphology of the resulting micelles changed from irregular, to spherical, ellipsoidal, and finally, cylindrical.[16] These works highlight the important relationship between polypeptide side chain structure, secondary conformation, and nanoparticle morphology.

A variety of other moieties have also been used to modify the side chains of synthetic polypeptide materials (reviewed elsewhere[17]), however, pyridines represent an underutilised class of compounds for this purpose. Three pyridine regioisomers exist, classified depending on the

position of their nitrogen heteroatom: *para* (4 position), *meta* (3 position) or *ortho* (2 position), giving rise to polymers with subtle structural differences. Materials containing pyridine functional groups have been extensively investigated in the polymer field for biomaterial applications, largely owing to their pH-responsive nature and antimicrobial effects. For example, pH-responsive micelles containing poly(2-vinylpyridine) (P2VP) or poly(4-vinyl pyridine) (P4VP) blocks have been used to achieve controlled drug release under acidic conditions,[18, 19] while others have reported that pyridine-containing polymers can exhibit antimicrobial activity.[20, 21] It is possible therefore, that modification of polypeptide materials with these groups may impart them with these useful properties for pharmaceutical applications. However, despite the appealing properties of pyridine moieties, these functional groups have not been explored for the side-chain modification of polymer-homopolypeptide materials.

Building on the existing body of work, we aimed to prepare polymer-homopolypeptide micelles modified with pyridine groups to investigate how subtle changes to the homopolypeptide side chain structure can influence micelle morphology. To our knowledge, there have been no published examples that investigate the interplay between the structure of the side chains of polymer-homopolypeptides when the polypeptide pendant groups are regioisomers, their resulting secondary conformations, and subsequent micelle morphology. Exploring this relationship is crucial towards understanding how the overall size and shape of polypeptide-based micelles can be tuned through synthetic modifications, which is of particular importance for mediating and directing specific interactions with biological systems.[22] Micelles of worm-like morphology, for example, have been shown to exhibit higher cell uptake or deeper penetration into multicellular tumour spheroids compared to spherical micelles.[23, 24]

Therefore, to explore the influence of regioisomeric pendant groups on the secondary structure of polymer-homopolypeptide diblock copolymers and the morphology of their micelles, we prepared a series of PEG-*b*-PMG copolymers by grafting *para*-, *meta*- or *ortho*-(hydroxymethyl)pyridines to PEG-*b*-PGA. Our findings suggest that the position of the pyridyl heteroatom influenced the dominant secondary structure of the polypeptide, which was associated with changes in the micelle size and shape, ranging from ellipsoids to elongated discs and cylinders when prepared by a film hydration method. While this study focused on the regioisomer-structure relationships of the polymers, the PEG-*b*-PMG copolymers are also of interest for the development of pH-responsive micelles for endosomal-lysosomal drug delivery due to the pH-responsive properties of the pyridine groups, which will be reported on in future studies.

Experimental

Materials

γ-Benzyl-L-glutamate (≥ 99%), 4-(hydroxymethyl)pyridine (99%), 3-(hydroxymethyl)pyridine (98%), 2-(hydroxymethyl)pyridine (98%), 4-(dimethylamino)pyridine (DMAP; ≥ 99%), *N,N′*-dicyclohexylcarbodiimide (DCC; 99%), anhydrous pentane, anhydrous dimethyl formamide (DMF), chloroform-d ($CDCl_3$; 99.8% D atom), dimethyl sulfoxide-d_6 (DMSO-d_6; > 99.8% D atom), methanol-d_4 (CD_3OD; > 99.8% D atom), deuterium oxide (D_2O; 99.9% D atom), deuterium chloride solution (DCl; 35 wt%, 99% D atom), and sodium deuteroxide (NaOD; 30 wt%, 99% D atom) were procured from Sigma-Aldrich. Analytical reagent (AR) grade tetrahydrofuran (THF), dichloromethane (DCM), diethyl ether, magnesium sulphate ($MgSO_4$), sodium hydroxide pellets (NaOH), potassium hydroxide (KOH), sodium chloride (NaCl), potassium chloride (KCl), hydrochloric acid (HCl; 37% w/w), ethyl acetate (EtOAc), methanol (MeOH), sodium azide (> 99%), and acetic anhydride (> 98%) were obtained from ChemSupply. THF was dried over 3Å molecular sieves before use. α-Methoxy-ω-amino PEG hydrochloride salt (PEG-NH_2; amine substitution ≥ 95% (experimentally confirmed by proton (^1H) nuclear magnetic resonance (NMR) spectroscopy at 97% amine substitution); supplier molecular weight = 10 kDa, number-average molecular weight ($M_{n,\ NMR}$) = 8.3 kDa) was purchased from JenKem Technology USA. Triphosgene (> 98%) was sourced from TCI Chemicals. Spectra-Por® 6 regenerated cellulose dialysis tubing (molecular weight cut-off (MWCO) = 2 kDa) was acquired from Pacific Laboratory Products. Phosphate buffered saline (PBS; 10 mM) solutions were prepared using Gibco™ PBS tablets purchased from ThermoFisher Scientific. Sodium acetate (> 99%) was supplied by Ajax FineChem. Ultrahigh-purity argon (99.999%) was purchased from BOC. Uranyl acetate (2% w/v, in ultra-pure water) was supplied by ProSciTech. Carbon-coated copper grids

(200-mesh) were purchased from Ted Pella. Ultrapure water (resistivity ≥ 18 MΩ.cm) was sourced directly from a Sartorius Arium Pro Ultrapure Water System. Tzero aluminium differential scanning calorimetry (DSC) pans and hermetic aluminium thermogravimetric analysis (TGA) pans were purchased from DSC Consumables Inc. Narrow dispersity (*Đ*) gel permeation chromatography (GPC) PEG standards were purchased from Polymer Standards Service GmbH. All chemicals were used as received, unless otherwise specified.

Methods

Instrumentation

^{1}H and ^{13}C NMR spectroscopy were performed at 298 K using a 500 MHz Bruker NMR AVANCE III HD NMR spectrometer, operating at 500 and 126 MHz, respectively. Samples were dissolved in deuterated $CDCl_3$, DMSO-d_6, CD_3OD, or D_2O, where specified, using the residual solvent peak as an internal reference.[25] The NMR spectra were analysed using MestReNova (v14.2.0). Degree of substitution (DS) values were calculated from ^{1}H NMR spectra *via* integration of the aromatic pyridine protons (δ_H 7–8 ppm) compared to the methine proton of the polypeptide repeat unit (RU) (δ_H ~ 4.0 ppm), using the following equation:

$$\text{DS (\%)} = \frac{Integration\ of\ aromatic\ protons}{No.aromatic\ protons \times (Integration\ of\ methine\ proton)} \times 100\%$$

GPC was performed on two Shimadzu liquid chromatography systems, each coupled to UV-vis (SPD-10A) and differential refractive index (RID-20A, λ = 633 nm) detectors, using mobile phase compositions of either THF (at a flow rate of 1 mL/min), or 50% MeOH aqueous solution in 0.05 M NaCl (at a flow rate of 0.8 mL/min), where specified. Separation by organic-phase GPC was achieved using Shimadzu GPC8025D and GPC-80MD columns in series. Aqueous-phase GPC was performed using Agilent PL aquagel-OH MIXED-M (8 μm) and PL aquagel-OH 20 (5 μm) columns in series. GPC sample concentrations were ~ 5 mg/mL.

TGA was conducted on a TA Instruments Discovery TGA5500 under nitrogen (sample purge flow rate = 25 mL/min). Samples (~ 10 mg) were measured into aluminium pans and analysed between 25–600 °C at a ramp rate of 10 °C/min. DSC of polymer samples (~ 5 mg) was performed on a TA Instruments DSC250 using standard Tzero aluminium pans. Samples were subjected to a heat-cool-heat cycle between -80 to 180 °C at a ramp rate of 5 °C /min under a continuous flow of nitrogen (cell purge flow rate = 50 mL/min). Data analysis was performed using TA Universal Analysis software (v4.5A).

Fluorimetry for the determination of critical micelle concentrations (CMCs) were conducted on a Shimadzu RF-6000 fluorescence spectrophotometer at 22 ± 1 ℃ using a four-sided polished quartz cuvette (4 mL, 10 mm pathlength). Fluorescence measurements were recorded between 350–470 nm at a scan speed of 2000 nm/min and 3.0 nm bandwidth following excitation at λ_{ex} = 334 nm.

DLS was performed on a Malvern Panalytical Zetasizer Nano ZS in low volume (1 mL) polystyrene cuvettes. The micelle particle size distributions (PSDs) were recorded following equilibration at 25 °C for 25 s. All measurements were performed in triplicate.

TEM was performed on a FEI Tecnai G2 Spirit transmission electron microscope using carbon-coated copper grids (200-mesh). The carbon-coated copper grids were plasma treated (air) for 30 s, then an aliquot of the micelle solution (5 μL) was deposited on the grid for 2 min before being gently wicked away using filter paper. Negative staining was performed using uranyl acetate (2% w/v) solution (5 μL), deposited for 30–60 s, after which the staining solution was wicked away and the samples directly analysed. The average length/diameter of the particles from TEM were measured manually using ImageJ software (v1.8.0_345)[26] after digital calibration of the scale.

SAXS experiments were conducted at the SAXS/WAXS beamline of the Australian Synchrotron [Australian Nuclear Science and Technology Organisation (ANSTO), Clayton, Victoria].[27] Experiments were performed using the sample autoloader, where measurements were recorded in a fixed quartz glass capillary of 0.9–1.25 mm diameter and 0.01–0.03 mm wall thickness (sample volume = 100 μL). Each sample was preceded by one blank buffer wash and thoroughly aspirated with water and Hellmanex solution (3×) to avoid cross-contamination between samples. The experiments were run at 25 °C using ~ 25% of the total flux of the beamline. Two detector configurations were used: (i) photon energy = 12.0 keV (wavelength, λ = 1.03 Å); sample to detector distance = 900 mm, and (ii) photon energy = 12.0 keV (wavelength, λ = 1.03 Å), sample to detector distance = 7290 mm. 2D scattering patterns were recorded using a Dectris Pilatus 2M detector and data reduction was performed using the in-house developed software, Scatterbrain. Data from the two detector configurations were background subtracted in Scatterbrain (v2.820), then stitched into a continuous scattering profile with q-range = 0.017–1.59 $Å^{-1}$ using ATSAS Primus (version 3.0.5). Form-factor modelling was performed using SASView (version v5.0.4). A series of micelle solutions with varying polymer (0.5, 1, 2, 5 and 10 mg/mL) and salt (0, 50, 100, 154 mM KCl) concentration gradients were initially investigated to identify the optimal conditions to maximise the signal-to-noise ratio and minimise structure factor effects (i.e., secondary aggregation and interparticle repulsion; Supplementary Information (SI), **Figure S10**). In all cases, a salt concentration of 154 mM KCl was found to minimise the interparticle repulsion arising from the cationic nature of the polymers at pH 2.5. The optimal concentrations for PEG-*b*-PMG and PEG-*b*-PBG micelles was determined to be 1 and 0.5 mg/mL, respectively. Following the self-assembly procedures outlined above, the resulting pH of the samples was

recorded, and the final dialysate collected for use in background measurements for subsequent SAXS experiments.

CD spectroscopy was performed on a JASCO-815 CD spectrometer using a quartz cuvette (path length 1 mm), at ambient temperature. Samples for CD experiments were prepared by a 1:5 dilution of the SAXS samples above with ultrapure water. Data was therefore recorded at polymer concentrations of 0.2 mg/mL (PEG-*b*-PMG) or 0.1 mg/mL (PEG-*b*-PBG), and final salt concentration of 31 mM KCl. Samples were recorded using a quartz cuvette with a path length of 1 mm at ambient temperature. Spectra were recorded between 193–250 nm under standard sensitivity settings, with a scanning speed of 100 nm/min, data pitch of 0.5 nm, digital integration time of 4 sec, and 3 accumulations per sample.

ATR-FTIR spectroscopy was performed on micellised and lyophilised PEG-*b*-PBG and PEG-*b*-PMG copolymers to preserve the secondary conformation. Micelles were prepared according to the preparation methods outlined below, then frozen to –80 °C. The water was removed by lyophilisation (–50 °C, 0.35 mbar) over 48 h using a Martin Christ GmBH Alpha 1-2 LDplus freeze drier. FTIR spectra were measured on a Perkin Elmer Spectrum Two FTIR Spectrometer equipped with a diamond ATR crystal. Data were collected in the spectral range of 400–4000 cm^{-1} from 4 scans with a resolution of 4 cm^{-1}. FTIR measurements were performed on micellised and lyophilised polymer powders by loading directly onto the ATR crystal, using ambient air as a background. Transmittance (%) data was then converted to absorbance using the following equation:

$$Absorbance = 2 - log_{10}(\frac{1}{\%\ Transmittance})$$

To improve the signal-to-noise ratio of the absorbance data, a 4-point Savitsky–Golay smoothing was applied before calculating the second derivative of the data using GraphPad Prism (v9.5.1).

To deconvolute the data, the second derivative of the absorbance data was calculated as a means of resolving the individual bands to aid in the identification of hidden peaks, whereby peak minima in the second derivative spectra corresponded to local maxima in the original spectrum. Based on the minima identified in the second derivative data, curve fitting of the amide I peak (1600–1700 cm^{-1}) was then performed using Fityk software (v1.3.1).[28] Firstly, background subtraction was performed using the 'baseline mode' function by selecting the minima either side of the amide I peak in the FTIR absorbance spectra, thereby setting these values to 0. Curve fitting and fit optimisation were performed using the Voigt function in Fityk software (v1.3.1), by fixing the centre of the peaks to the minima observed in the second derivative plots and fixing the peak shape to 1.0. The peak width and peak height were left as free parameters to be optimised by the software. The secondary structures represented by each peak were then assigned based on literature frequencies and assignments.[29] Quantification was performed by calculating the area of the peaks corresponding to each secondary structure in the amide I region, with respect to the total area of the peaks in this region.

Synthesis of γ-benzyl-L-glutamate NCA

γ-Benzyl-L-glutamate NCA was synthesised as previously reported with modification.[30] To a stirred suspension of *γ*-benzyl-L-glutamate (5.01 g, 20.9 mmol) in anhydrous THF (315 mL) in a pear-shaped flask (500 mL) under argon was added triphosgene (3.20 g, 10.8 mmol) at 21 ± 1 °C. The reaction mixture was stirred vigorously at 65 °C for 30 min; completion of the reaction was marked by the formation of a clear solution after ~ 15 min. After cooling to ambient temperature, the solvent was removed *in vacuo* and the resulting solid was triturated twice with anhydrous pentane (60 mL). After decanting the supernatant, the product was further dried under high vacuum (0.1 mbar, 22 ± 1 °C) to give *γ*-benzyl-L-glutamate NCA as a white powder (5.37 g,

97%). ^{1}H NMR (500 MHz, $CDCl_3$): δ_H 7.45–7.31 (*m*, 5H, Ar**H**), 6.45 (*br. s*, 1H, N**H**), 5.14 (*s*, 2H, C**H**$_2$O), 4.40 (*t*, *J* = 6.6 Hz, 1H, NH-C**H**), 2.63 (*t*, *J* = 6.9 Hz, 2H, O(CO)C**H**$_2$CH$_2$), 2.31 (*m*, *J* = 14.7 Hz, 1H, O(CO)CH$_2$C**H**$_2$), 2.12 (*m*, *J* = 14.3 Hz, 1H, O(CO)CH$_2$C**H**$_2$) ppm (**Figure 1**). ^{13}C NMR (126 MHz, $CDCl_3$) δ_C 172.8 (NH**C**O), 169.7 (O**C**=O), 151.9 (CH**C**=O), 135.6 (Ar**C**H), 129.1 (Ar**C**H), 129.0 (Ar**C**H), 128.9 (Ar**C**H), 128.8 (Ar**C**H), 128.5 (Ar**C**H), 67.6 (ArCH-**C**H), 57.4 (**C**HC=O), 30.4 (NH**C**H), 27.4 (CH$_2$**C**H$_2$CH) ppm (SI, **Figure S1**).

Synthesis of PEG-*b*-PBG

γ-Benzyl-L-glutamate NCA (1.83 g, 6.93 mmol) was dissolved in anhydrous DMF (70 mL) in a two-necked round bottom flask (250 mL) under argon and PEG-NH$_2$ was added (1.39 g, 139 µmol, monomer to initiator ratio ([M]/[I]) = 50). After stirring at 21 ± 1 °C for 72 h, acetic anhydride (140 µL, 1.48 mmol, 10 eq. relative to initiator) was added and the reaction was stirred for 1 h to endcap the terminal amine group of the copolymer. The crude reaction mixture was precipitated directly into diethyl ether (700 mL) and the solid precipitate was isolated by centrifugation (6 krpm, 5 min). The resulting polymer pellet was redissolved in DCM (20 mL), precipitated into diethyl ether (200 mL) and isolated by centrifugation (6 krpm, 5 min); this step was repeated five times. The solid was then dried under high vacuum (0.1 mbar, 22 ± 1 °C) for 16 h to obtain PEG-*b*-PBG as a white powder (2.82 g, 97%). GPC (in THF, calculated relative to narrow *Đ* PEG standards): weight-average molecular weight ($M_{w,GPC}$) = 10.3 kDa, $M_{n,\,GPC}$ = 9.9 kDa, *Đ* (M_w/M_n) = 1.04. ^{1}H NMR (500 MHz, $CDCl_3$) δ_H 8.14–8.54 (*br. s*, N**H**, PBG RU), 7.16–7.36 (*br. m*, Ar**H**, PBG RU), 4.92–5.19 (*br. s*, C**H**$_2$O, PBG RU), 3.83–4.09 (*br. s*, C**H**NH, PBG RU), 3.65 (*s*, C**H**$_2$C**H**$_2$O, PEG RU), 2.61–2.13 (*br. m*, C**H**$_2$C**H**$_2$, PBG RU) ppm; $M_{n,\,NMR}$ = 15.3 kDa.

Synthesis of PEG-*b*-PGA

To a solution of PEG-*b*-PBG (4.08 g, 194 μmol) in THF (240 mL) in a round bottom flask (500 mL) was added 1.0 M NaOH (12.5 mL, 12.5 mmol, 1.50 eq. per RU) dropwise. The reaction mixture was stirred at 21 ± 1 °C for 18 h and then acidified by the addition of 2.0 M HCl (10.0 mL). The reaction mixture was concentrated *in vacuo*, then transferred to regenerated cellulose dialysis tubing (MWCO = 2 kDa) and dialysed over 96 h against ultrapure water (9 × 3 L) and then 0.01 M HCl (1 × 2 L) to ensure protonation of the carboxylic acid pendant groups. The contents of the dialysis tubing were concentrated, then dried under vacuum (0.1 mbar, 22 ± 1 °C) to afford PEG-*b*-PGA as a white solid (2.33 g, 72%). GPC (in 50% MeOH with 0.05 M NaCl, calculated relative to narrow *Đ* PEG standards): $M_{w,\,GPC}$ = 11.2 kDa, $M_{n,\,GPC}$ = 10.4 kDa, *Đ* (M_w/M_n) = 1.07. ^{1}H NMR (500 MHz, DMSO) δ_H 12.0–12.2 (*br. s*, COO**H**, PGA RU), 7.91–8.21 (*br. m*, N**H**, PGA RU), 4.08–4.42 (*br. s*, C**H**NH, PGA RU), 3.50 (*s*, C$\mathbf{H}_2$C$\mathbf{H}_2$O, PEG RU), 2.06–2.37 (*br. s*, C$\mathbf{H}_2$COOH, PGA RU), 1.91–1.74 (*br. m*, CHC$\mathbf{H}_2$, PGA RU) ppm; $M_{n,\,NMR}$ = 12.2 kDa.

Synthesis of PEG-*b*-4PMG

4-(Hydroxymethyl)pyridine (1.09 g, 9.98 mmol) was melted at 60 °C in a round bottom flask (25 mL) and PEG-*b*-PGA (102 mg, 71.0 μmol) was added with stirring. DMSO (220 μL) was added to the reaction mixture to facilitate dissolution of the polymer. DCC (109 mg, 529 μmol) and DMAP (30.4 mg, 249 μmol) were added sequentially, and the reaction was stirred at 60 °C for 45 h. After cooling to 21 ± 1 °C, the crude reaction mixture was precipitated into cold EtOAc (–20 °C, 12 mL), and the precipitate was isolated by centrifugation (6 krpm, 2 min). After decanting the supernatant, the polymer was redissolved in methanol (1 mL), precipitated into diethyl ether (10 mL) and the precipitate was isolated *via* centrifugation (6 krpm, 2 min); this step was repeated eight times to remove the residual *N*,*N*'-dicyclohexylurea (DCU). The product was dried under high vacuum (0.1 mbar, 22 ± 1 °C) for 18 h to afford PEG-*b*-4PMG, 100 mg (80%).

GPC (in 50% MeOH with 0.05 M NaCl, calculated relative to narrow *Đ* PEG standards): $M_{w,\,GPC}$ = 8.7 kDa, $M_{n,\,GPC}$ = 6.5 kDa, *Đ* (M_w/M_n) = 1.33. ^{1}H NMR (500 MHz, 15% *v/v* 1 M DCl in D_2O) δ_H 8.63–8.76 (*br. s*, Ar**H**, 4PMG RU), 7.89–8.05 (*br. s*, Ar**H,** 4PMG RU), 5.29–5.50 (*br. s*, Ar-C**H**$_2$, 4PMG RU), 4.18–4.42 (*br. s*, C**H**NH, 4PMG RU), 3.62 (*s*, $CH_2C\mathbf{H}_2O$, PEG RU), 2.82–1.86 (*br. m*, $C\mathbf{H}_2CH_2$, 4PMG RU) ppm; $M_{n,\,NMR}$ = 14.6 kDa.

General procedure for synthesis of PEG-*b*-2PMG and PEG-*b*-3PMG

PEG-*b*-PGA (663 mg, 50.0 μmol) was dissolved in a large excess of the 2-(hydroxymethyl)pyridine or 3-(hydroxymethyl)pyridine (40 eq. per RU, 5 mL). DCC (516 mg, 2.50 mmol) and DMAP (153 mg, 1.25 mmol) were added sequentially, and the reaction performed neat at 60 °C for 45 h. The crude reaction mixture was precipitated in EtOAc cooled to –20 °C (40 mL), and isolated by centrifugation at 6 krpm for 2 min. After decanting the supernatant, the polymer was redissolved in methanol (5 mL) and precipitated into diethyl ether (50 mL) and the precipitate was isolated *via* centrifugation (6 krpm, 2 min); this step was repeated five times to remove the residual DCU. The product was dried under high vacuum (0.1 mbar, 22 ± 1 °C) for 3 d to afford PEG-*b*-2PMG (605 mg, 64%) and PEG-*b*-3PMG (512 mg, 66%) as off-white solids.

PEG-*b*-3PMG: GPC (in 50% MeOH with 0.05 M NaCl, calculated relative to narrow *Đ* PEG standards): $M_{w,\,GPC}$ = 9.4 kDa, $M_{n,\,GPC}$ = 7.8 kDa, *Đ* (M_w/M_n) = 1.22. ^{1}H NMR (500 MHz, DMSO-d_6) δ_H 8.41–8.64 (*br. m,* Ar**H**, 3PMG RU), 7.95–8.26 (*br. s*, N**H,** 3PMG RU), 7.62–7.82 (*br. s,* Ar**H**, 3PMG RU), 7.24–7.41 (*br. s*, Ar**H**, 3PMG RU), 4.96–5.19 (*br. s*, C**H**$_2$-Ar, 3PMG RU), 4.15–4.39 (*br. s*, C**H**$_2$NH$_2$, 3PMG RU), 3.50 (*s*, C**H**$_2$C**H**$_2$O, PEG RU), 2.25–2.44 (br. s, $CH_2C\mathbf{H}_2O$, PEG RU), 1.61–2.02 (*br. m*, $C\mathbf{H}_2CH_2$, 4PMG RU) ppm; $M_{n,\,NMR}$ = 14.0 kDa.

PEG-*b*-2PMG: GPC (in 50% MeOH with 0.05 M NaCl, calculated relative to narrow *Đ* PEG standards): $M_{w,\,GPC}$ = 9.3 kDa, $M_{n,\,GPC}$ = 7.6 kDa; *Đ* (M_w/M_n) = 1.20. ^{1}H NMR (500 MHz,

15% *v/v* 1 M DCl in D_2O) δ_H 8.63–8.73 (*br. s*, Ar**H**, 2PMG RU), 8.45–8.57 (*br. s*, Ar**H**, 2PMG RU), 7.89–8.03 (*br. m*, Ar**H**, 2PMG RU), 5.34–5.49 (*br. s*, Ar-C**H**$_2$, 2PMG RU), 4.14–4.34 (*br. s*, C**H**NH, 2PMG RU), 3.60 (*s*, $CH_2C\mathbf{H}_2O$, PEG RU), 2.64 – 1.82 (*br. m*, $C\mathbf{H}_2CH_2$, 2PMG RU) ppm; $M_{n,\,NMR}$ = 15.0 kDa.

PEG-*b*-PMG polymeric micelle assembly

PEG-*b*-PMG micelles were prepared by a film hydration procedure, according to the following general method. An aliquot (1 mL) of polymer stock solution (1 mg/mL, prepared in AR grade methanol) was transferred to a round bottomed flask (10 mL). The methanol was then removed, whilst rotating (200 rpm) under vacuum using a rotary evaporator to generate a thin film on the surface of the round bottomed flask. The thin film was then further dried under high vacuum at 0.1 mbar for 16 h. The copolymer films were then reconstituted in 154 mM KCl (1 mL) at pH 7.4 and equilibrated on an orbital shaker for 72 h to afford a final polymer concentration of 1 mg/mL. The solution was transferred into a Float-a-Lyzer device (MWCO 3.5–5k) and dialysed against 154 mM KCl, pH 7.4 (80 mL × 3) over 48–72 h.

PEG-*b*-PBG polymeric micelle assembly

Due to the poor aqueous solubility of PEG-*b*-PBG, the film hydration method could not be employed as precipitation of the polymer was observed. Therefore, an alternative self-assembly technique, solvent evaporation, was employed in addition to using a lower polymer concentration to avoid precipitation. Specifically, an aliquot (1 mL) of PEG-*b*-PBG stock (prepared in AR grade THF at 0.5 mg/mL) was transferred to a glass vial (4 mL). 154 mM KCl (1 mL) at pH 7.4 was added dropwise with gentle agitation to ensure homogeneity. The THF was then removed over 1–2 h on a dry block heater at 65 °C. Residual organic solvent was then removed under high vacuum (0.1 mbar) for 1 h. The solutions were then made up to a volume of 1 mL with water to afford a

final polymer concentration of 0.5 mg/mL. The solution was transferred into a Float-a-Lyzer device (MWCO 3.5–5 kDa) and dialysed against 154 mM KCl pH 7.4 (80 mL × 3) over 48–72 h.

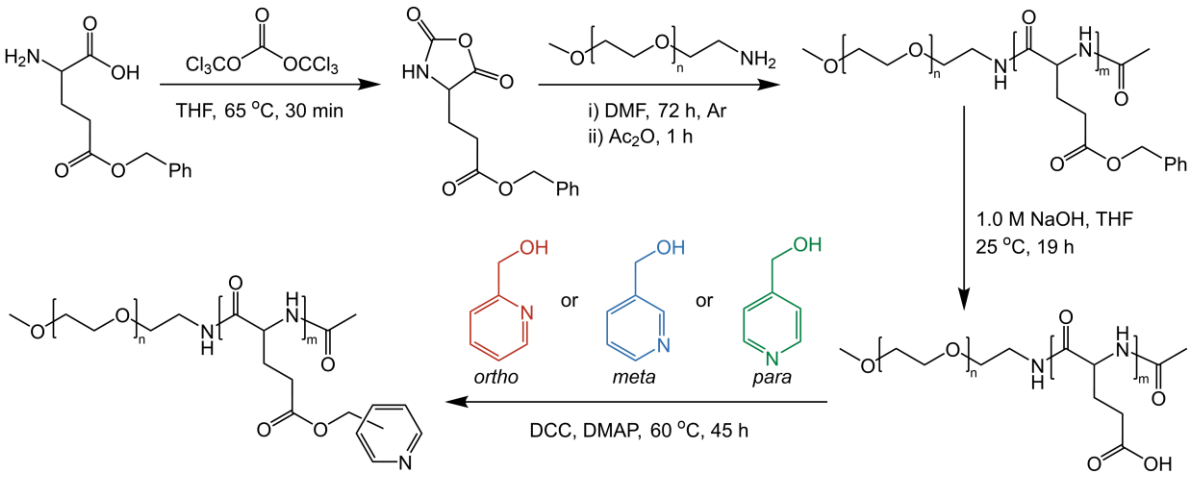
CMC determination of micelles by fluorimetry

The CMCs were determined by fluorimetry using pyrene as a fluorescent probe.[31-33] Stock solutions of pyrene (6×10^{-5} M) and the polymers (0.5 or 2 mg/mL) were prepared in methanol. Polymer solutions with concentrations ranging from 1×10^{-6} to 2 mg/mL (PEG-*b*-PMGs), or 2×10^{-7} to 0.5 mg/mL (PEG-*b*-PBG), were prepared by serial dilution of the stock solutions with methanol and transferred to separate round bottomed flasks (10 mL). Aliquots of the pyrene stock solution (50 μL) were transferred to each flask with agitation and the methanol was removed *in vacuo* on a rotary evaporator to generate thin films. The films were dried under high vacuum for 0.5–1 h to remove residual solvent, before being reconstituted in PBS (pH 7.4, 5 mL) to afford a final pyrene concentration of 6×10^{-7} M. The ratio of the intensities of the vibronic bands at λ_{em} = 372 and 384 nm (I_3/I_1) were plotted as a function of polymer concentration, where the CMC was defined as the intersect of the two slopes in the intensity *versus* concentration plot (SI, **Figure S5**).

Results and Discussion

Polymer synthesis and characterisation

A library of PEG-*b*-PMG copolymers were synthesised *via* grafting of *ortho-, meta-* or *para*-(hydroxymethyl)pyridine derivatives to a common PEG-*b*-PGA precursor, which in turn was prepared from the hydrolysis of a PEG-*b*-PBG diblock copolymer (**Scheme 1**). The synthesis of the PEG-*b*-PMG copolymers was followed by ^{1}H NMR spectroscopy and GPC.



Scheme 1. Synthesis of PEG-*b*-PMG copolymers *via* ROP of γ-benzyl-L-glutamate NCA to afford a PEG-*b*-PBG diblock copolymer, followed by base-catalysed hydrolysis and conjugation of hydroxymethyl pyridine derivatives *via* carbodiimide coupling.

Initially, PEG-*b*-PBG was prepared *via* the ROP of γ-benzyl-L-glutamate NCA (**Figure 1** and SI, **Figure S1**) using a PEG-NH_2 macroinitiator ($M_{n,\ NMR}$) = 8.3 kDa) at a [M]/[I] of 50. The polymerisation was quenched with acetic anhydride with the intention to acetylate the terminal amine of the growing chain and prevent undesirable cross-linking reactions in subsequent steps. The formation of PEG-*b*-PBG was marked by the appearance of characteristic broad signals in the ^{1}H NMR spectrum (**Figure 1A**) corresponding to the PEG (δ_H = 3.65 ppm) and PBG (δ_H = 7.26,

5.04, 3.94 and 2.13–2.61 ppm) RUs.[34] Comparison of the RU integrations revealed a $M_{n,\,NMR}$ of 15.3 kDa, which equated to a PBG DP of 37 (**Table 1**). This value was lower than the theoretical DP of 50 based on the initial [M]/[I] ratio, likely resulting from termination of the active end-groups due to intramolecular cyclisations and the subsequent formation of 'dead' pyroglutamate end-groups, as previously reported.[35, 36] This was supported by ^{1}H NMR spectroscopy of the reaction supernatant after ~ 72 h, which revealed the presence of unreacted NCA monomer and indicated that it was not completely consumed during the polymerisation reaction (SI, **Figure S2**). The presence of benzyl alcohol, formed as a by-product of intramolecular cyclisation reactions, was further evidenced by the appearance of additional resonances in the aromatic region of the ^{1}H NMR spectrum of the supernatant (SI, **Figure S2**).

The probability of these cyclisation reactions was further substantiated by GPC using a differential refractive index (DRI) detector (**Figure 1B**), which exhibited a primary peak at a retention volume of ~ 18.3 min that did not appear to return to the baseline before elution of the solvent front. The tailing at high retention volumes is ascribed to the formation of short oligomers of varying molecular weight by benzyl alcohol-initiated ROP. This contributed to a high apparent $Đ$ of 1.99 (integrated over retention volumes of 17.4–21.6 mL), which is significantly higher than those reported for PEG-*b*-PBG previously.[13] The higher extent of side reactions may be attributed to the ambient reaction temperature used during polymerisation, since fewer 'dead' polymer chains have been reported when the ROP reaction was performed at reduced temperatures.[35, 37] Additionally, only a subtle shift in the peak to lower retention volumes was observed as compared to the PEG-NH_2 macroinitiator (SI, **Figure S3**). The presence of oligomers may contribute to an overestimation of the DP by ^{1}H NMR spectroscopy due to overlapping signals with the polymer, and therefore, it is possible that the actual DP of the PEG-*b*-PBG is lower than the calculated value

of 37. Additionally, despite the addition of acetic anhydride to endcap the terminal amine groups, the corresponding methyl signal could not be readily observed in the ^{1}H NMR spectrum (δ_H ~ 2 ppm). This further supports that pyroglutamate formation had likely occurred, which would result in the absence of a free amine end-group required for acetylation by the acetic anhydride. Together, these findings suggest that it is likely that intramolecular cyclisation side reactions had taken place, which contributed to a lower than anticipated DP for the PEG-*b*-PBG copolymer. However, considering that the oligomers were removed during dialysis in the subsequent step, they were not thought to be a critical factor influencing subsequent analyses.

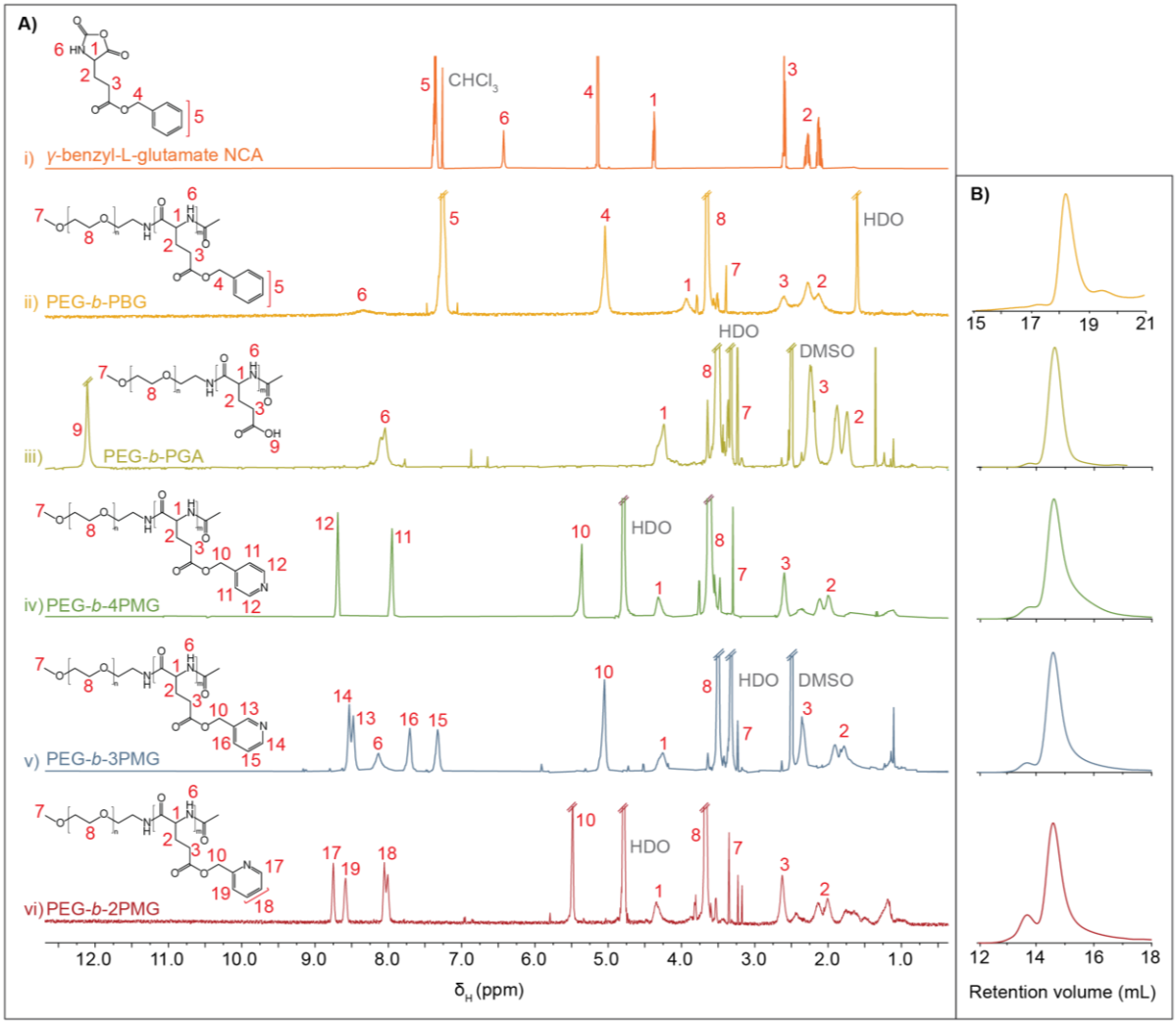


Figure 1. **A)** Stacked ^{1}H NMR spectra (500 MHz, 298 K) of (i) γ-benzyl-L-glutamate NCA ($CDCl_3$), (ii) PEG-*b*-PBG ($CDCl_3$), (iii) PEG-*b*-PGA (DMSO-d_6), (iv) PEG-*b*-4PMG (0.15 M DCl in D_2O), (v) PEG-*b*-3PMG (DMSO-d_6), and (vi) PEG-*b*-2PMG (0.15 M DCl in D_2O) and **B)** corresponding GPC DRI chromatograms. GPC of the polymers was run in 0.05 M NaCl in 1:1 *v/v* methanol:water, with the exception of PEG-*b*-PBG, which was run in THF.

In the subsequent reaction, base-catalysed hydrolysis of the benzyl protecting groups of PEG-*b*-PBG proceeded quantitatively to afford PEG-*b*-PGA. Successful deprotection was marked by the loss of signals at δ_H = 7.26 and 5.04 ppm corresponding to the benzyl protecting groups and the appearance of a characteristic signal at ~ δ_H = 12 ppm corresponding to the carboxylic acid protons. Comparison of the RU integrations for PEG-*b*-PGA provided a $M_{n,\,NMR}$ = 12.2 kDa, which equated to a PGA DP of 22 (**Table 1**). Additionally, GPC revealed a decrease in dispersity ($Đ$ = 1.07, integrated over a retention volume of 13.3–16.2 mL) compared to the PEG-*b*-PBG precursor ($Đ$ = 1.99), coinciding with removal of the oligomers during dialysis.

The *ortho-, meta-* and *para*-(hydroxymethyl)pyridine derivatives were subsequently grafted to the pendant carboxylic acid groups of PEG-*b*-PGA *via* carbodiimide coupling to afford the PEG-*b*-#PMG copolymers, whereby # designates the regioisomers; *ortho* (2 position), *meta* (3 position) and *para* (4 position). Since all PEG-*b*-PMG polymers were generated from the same PEG-*b*-PGA precursor, in theory the only changing variable was the position of the pyridine heteroatom. This assumes that the polymer molecular weight (i.e., chain length, polypeptide fraction) and DS are similar across all PEG-*b*-PMG copolymers. Initially, the reaction was optimised using a variety of coupling reagents (SI, **Table S1**), which revealed that the highest DS was obtained when the reaction was performed in the presence of a large excess of the hydroxymethyl pyridine derivative. Successful conjugation of the hydroxymethyl pyridine

derivatives to the PEG-*b*-PGA copolymer was confirmed by the appearance of signals between δ_H = 5–5.5 and 7–9 ppm in the ^{1}H NMR spectra, corresponding to methylene protons adjacent to the ester/pyridyl groups and the aromatic pyridyl protons, respectively. Comparison of the integrations of the pyridyl signals relative to the methine signal of the polypeptide backbone allowed calculation of the DS, which were > 90% for all of the PEG-*b*-PMG copolymers (**Table 1**).

Comparison of the RU integrations calculated by NMR spectroscopy suggested that the DP of the PMG blocks decreased after the coupling reactions, potentially indicating cleavage of the polypeptide backbone. This coincided with an increase in $Đ$ to 1.20–1.33 (*cf.* PEG-*b*-PGA, integrated over a retention volume of ~ 13–18 mL) observed by GPC (**Figure 1B**). The PGA backbone may have been particularly susceptible to hydrolysis if pyroglutamate formation had occurred due to intramolecular cyclisation reactions, potentially facilitated by trace amounts of water or hydroxides present in the reaction mixture.[38] However, without further analysis of the polymer end groups and molecular weight distribution, this cannot be confirmed with certainty. An increase in the molecular weight distribution may influence the behaviours of the PEG-*b*-PMG copolymers, since low- and high- molecular weight polymers could exhibit differences in self-assembly properties and morphology.[39]

In addition, a secondary peak was also visible in the GPC traces of the PEG-*b*-PGA and PEG-*b*-PMG copolymers at ~ 13.7 mL, which may correspond to a population of polypeptides with α-helical domains. α-Helices have been associated with changes in hydrodynamic volume that can contribute to the formation of bimodal GPC distributions.[40] For example, Huesmann *et al.* previously reported that bimodal GPC traces were observed for poly(lysine)s due to a 1.6-fold increase in hydrodynamic volume of α-helices compared to polymer coils.[40] While these effects were reportedly less prominent in PGA, it may be possible that the small peak at a retention volume

of around 13.7 mL corresponds to population of α-helical secondary structures in the PGA and PMG blocks.

Table 1. Characterisation of PEG-*b*-PBG, PEG-*b*-PGA and PEG-*b*-PMG copolymers.

Polymer	$M_{n,\,NMR}$ (kDa)	Homopolypeptide DP[a]	$M_{n,\,GPC}$ (kDa)	$Đ$	DS (%)[b]	T_g (°C)[c]
PEG-*b*-PBG	15.3	37	9.9	1.99	-	23.8
PEG-*b*-PGA	12.2	22	10.4	1.07	-	121.6
PEG-*b*-4PMG	14.6	12	6.5	1.33	91	31.3
PEG-*b*-3PMG	14.0	15	7.8	1.20	>99	33.5
PEG-*b*-2PMG	15.0	14	7.6	1.22	96	35.2

[a] DP calculated with respect to integration of the pyridine protons relative to the methyl end-group signal in the ^{1}H NMR spectra. [b] DS calculated from ^{1}H NMR spectra *via* integration of the aromatic pyridine protons (δ_H 7–8 ppm) compared to the methine proton of the peptide RU ($\delta_H \sim 4.0$ ppm). [c] T_g values calculated from second heating cycle of DSC thermograms.

Thermal characterisation of the copolymers

The thermal properties of the copolymers were investigated by TGA (SI, **Figure S4**) and DSC (SI, **Figure S5**) to determine the thermal stability of the polypeptide block and investigate thermal transitions resulting from the copolymer morphology in the solid state, respectively. TGA thermograms revealed an absence of significant polymer degradation below 200 °C, with all copolymers exhibiting two clear degradation events. The PEG-*b*-PBG, PEG-*b*-PGA and PEG-*b*-PMG copolymers showed an initial mass loss of 13–30% between 240–270 °C, which may correspond to side chain decomposition. This is in agreement with the findings of Lillya *et al.*, who reported a PBG decomposition temperature of 246 °C, corresponding to pyrolysis of the polypeptide side chains.[41] Using gas chromatography, they identified that the major thermal decomposition products of PBG up to 325 °C were benzyl alcohol, toluene, benzaldehyde, and

benzoic acid, while for PGA, acetone, methanol and acetic acid were detected. A second apparent degradation event was visible at ~ 400 °C for all copolymers in the series. This degradation event was attributed to decomposition of the peptidic linkages,[42] with a likely contribution from the degradation of PEG.[43]

For all copolymers, DSC revealed the presence of a dominant endothermic peak between 50–60 °C upon heating, representing the melting temperature (T_m) of the PEG block (SI, **Figure S5**). A complementary exothermic peak corresponding to the PEG crystallisation temperature (T_{cryst}) was observed in the cooling cycle at ~ 30 °C for all copolymers. For the PEG-*b*-PBG copolymer, a small endothermic peak was observed at 109 °C on the first heating cycle and 90 °C on the second heating cycle, which has been previously ascribed to transformations between the 7/2 and 18/5 helical conformations.[44] Interestingly, these helical transformations were not observed in the second cycles of the PEG-*b*-PMG copolymers. An endothermic inflection was also noted at 24 °C for the PEG-*b*-PBG copolymer, corresponding to the glass transition temperature (T_g) of the PBG block.[44] Similarly, the PEG-*b*-PMG copolymers also exhibited a visible T_g in the second heating cycle, albeit shifted to higher temperatures of 31–35 °C (**Table 2**). This increase in the T_g values may be related to H-bonding of the pyridyl side chains (*cf.* benzylic side chains), leading to increased intermolecular interactions. The degree of crystallinity (X_c) of the PEG block was calculated by comparing the enthalpy of crystallisation (ΔH_{cryst}) of the copolymers to that of 100% crystalline PEG (SI, **Table S2**).[45] The PEG block was found to be significantly less crystalline in PEG-*b*-PBG (X_c = 38%) when compared to the PEG-*b*-PMG copolymers (X_c = 58–63%), which may result from the pyridyl groups eliciting stronger intermolecular interactions (i.e., H-bonds), leading to a more ordered structure that influences crystallisation of the PEG component.[46, 47]Alternatively, the higher DP of the polypeptide block in the PEG-*b*-PBG

copolymer may act to depress the T_{cryst} and X_c of the PEG block as has been observed for other block copolymers.[44] For example, PEG crystallisation in PBG-PEG-PBG triblock copolymers is significantly influenced by the DP of the polypeptide block, with longer polypeptide blocks inhibiting PEG crystallisation.[44] No obvious trend in X_c was observed with respect to the regioisomers.

Micelle formation and characterisation

The CMC of the copolymers were determined by fluorimetry using pyrene as a fluorescent probe (SI, **Figure S6**),[33] which provided values of 3.8, 68, 5.0 and 1.2 mg/L for the PEG-*b*-PBG, PEG-*b*-4PMG, PEG-*b*-3PMG and PEG-*b*-2PMG copolymers, respectively (**Table 2**). The higher hydrophobicity of PEG-*b*-PBG relative to the PEG-*b*-PMG copolymers was expected to result in lower CMC values. Indeed, the CMC for the PEG-*b*-PBG copolymer was lower than that of the PEG-*b*-4PMG and PEG-*b*-3PMG copolymers. Unexpectedly, the CMC of the PEG-*b*-2PMG copolymer appeared to be below the PEG-*b*-PBG copolymer. While this may be counterintuitive based on their chemical structures, this may be explained differences in core packing and solvation. For example, the core of the PEG-*b*-2PMG micelles may be more tightly packed and less solvated than the PEG-*b*-PBG micelles, resulting in a more hydrophobic environment that may manifest as a lower CMC. This may also explain the significantly higher apparent CMC for the PEG-*b*-4PMG copolymers, which may exhibit looser core packing and, therefore, a higher extent of core solvation. This is qualitatively supported by ^{1}H NMR spectroscopy experiments, performed in neutral aqueous solutions many orders of magnitude above the apparent CMC, which show greater resolution and signal intensity of the PMG block for the PEG-*b*-4PMG micelles, while the signals from the PMG block of PEG-*b*-2PMG micelles are barely distinguishable from the baseline noise,

suggestive of differences in core solvation (SI, **Figure S7**). More compact core packing of polymer micelles has previously been reported to result in a decrease in the CMC, attributed to enhanced hydrophobicity.[48] Therefore, it is plausible that differences in micelle core packing may lead to changes in core solvation, which influences the polarity of the core, and therefore, the fluorescence intensity of the pyrene. Unfortunately, these analyses could not be performed on the PEG-*b*-PBG micelles due to their low aqueous solubility below the concentration requirements for ^{1}H NMR spectroscopy. However, it should be noted that the I_3 and I_1 bands of PEG-*b*-PMGs did not show a drastic change in the absolute fluorescence intensity, as typically observed for other micelles with more hydrophobic core-forming blocks (e.g., PEG-*b*-polycaprolactone (PCL)), which is attributed to the relative polarity of the polypeptide core. It is possible that this also contributes to the unexpected trends in the CMC data.

The PEG-*b*-PBG and PEG-*b*-PMG copolymers were then self-assembled into micelles in aqueous solution (154 mM KCl, pH ~ 7), at a concentration well above the CMC, for subsequent characterisation of their morphology. The PEG-*b*-PMG micelles were prepared using a film hydration approach; however, this method could not be used for the PEG-*b*-PBG copolymer due to extensive precipitation, and therefore an alternative solvent evaporation method was employed. Hence, it is important to note that these differences in micellisation procedures (solvent evaporation *vs.* film hydration) between the PEG-*b*-PBG and PEG-*b*-PMG copolymers may have an influence on the observed micelle morphology (*vide infra*). Additionally, although the pyridine groups are ionisable, which could in theory contribute to micelle swelling or changes in morphology, they were expected to be predominantly unionised at neutral pH (> 99%, based on the approximate pK_a of the pyridine groups of ~ 5),[49] and therefore this was not thought to be a significant contributing factor.

Prior to discussion on micelle size, it is also important to highlight the theoretical differences in the size estimates obtained from each technique. For example, the hydrodynamic diameter (D_h) obtained from DLS is intensity-weighted, the average dimensions obtained from TEM are number-weighted, and the values determined from SAXS are volume-weighted. As a result, the sizes from each technique may not necessarily be directly comparable but still provide useful complementary information from which general trends can be discerned. Initial investigations into micelle size were performed using DLS, which revealed monomodal PSDs that provided D_h values of 57–114 nm, consistent with micellar structures (**Figure 2** and SI, **Figure S8**).

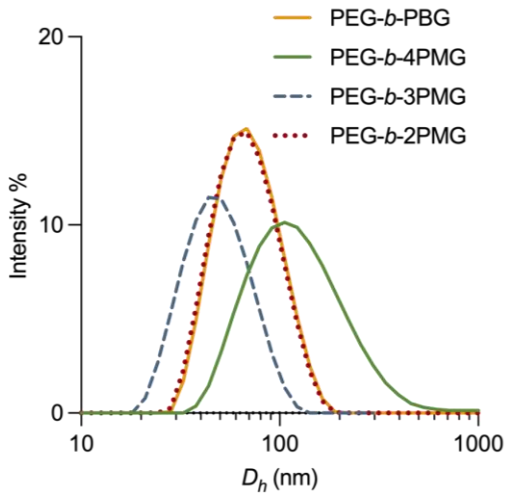


Figure 2. DLS intensity PSDs of the PEG-*b*-PMG and PEG-*b*-PBG copolymers in 154 mM KCl (pH ~7).

The D_h and polydispersity index (PDI) values of the micelles were generally similar across the entire series, with an average D_h around 57–65 nm and PDI around 0.12–0.13, with the exception of the PEG-*b*-4PMG micelles, which exhibited a significantly larger D_h and PDI (**Table 2**).

Interestingly, the PEG-*b*-PBG and PEG-*b*-2PMG micelles exhibited similar D_h values, despite their differences in hydrophobicity and DP, however, this may be explained by differences in core packing or morphology, which would not be detectable by DLS. Therefore, while DLS provided an estimate of the D_h of the micelles, it was limited in that it assumed a spherical morphology and could not offer any insights into the micelle shape. This is particularly important since block copolymers containing PEG and PBG have previously been reported to adopt micelles of various morphologies, including spheres, rods and cylinders.[44,13]

Table 2. Characterisation of PEG-*b*-PBG and PEG-*b*-PMG micelles via fluorimetry using pyrene as a probe, DLS, TEM and SAXS.

Polymer	CMC (mg/L)	Z-ave ± SD (nm)[a]	PDI[a]	TEM characterisation[b]			SAXS characterisation[c]	
				Morphology	Dimensions (nm)	ρ	Morphology	R_g (Å)
PEG-*b*-PBG	3.8	65.2 ± 1.3	0.13	Spherical	d = 68.6 ± 18.3	---	Ellipsoidal	167
PEG-*b*-4PMG	68	113.7 ± 1.5	0.25	Ellipsoidal	l = 189.8 ± 46.9 w = 26.4 ± 6.9	0.14	Rod/ platelet	---
PEG-*b*-3PMG	5.0	57.2 ± 1.9	0.12	Worm-like	l = 174.7 ± 44.1 w = 8.1 ± 2.6	0.05	Cylindrical	144
				Spherical	d = 40.1 ± 9.5	---	---	
PEG-*b*-2PMG	1.2	63.5 ± 0.6	0.13	Spherical	d = 75.1 ± 21.9	---	Ellipsoidal	170

[a] Z-average (intensity weighted mean D_h) and PDI as determined from DLS intensity PSDs in 154 mM KCl, pH 7.4 (n = 3). [b] TEM characterisation: dimensions (d = diameter, l = length, w = width) measured with reference to a digital magnification calibration, aspect ratio (ρ) calculated as width (nm) divided by length (nm). [c] SAXS characterisation: morphology based on modelling of theoretical form factors. Radius of gyration (R_g) estimated from Guinier analyses in ATSAS Primus.

To provide insights into the micelle shape, the morphology of the PEG-*b*-PMG and PEG-*b*-PBG micelles was investigated by TEM (**Figure 3** and SI, **Figure S9**). TEM revealed that when

the nitrogen atom was in the *para* position relative to the ester linkage, as in the case of PEG-*b*-4PMG, the micelles exhibited an elongated morphology consistent with rods or ellipsoids. Contrastingly, in the *meta* position, as in the case of PEG-*b*-3PMG micelles, there appeared to be a population of both long, worm-like structures and those with a more spherical morphology. In the *ortho* position (i.e., PEG-*b*-2PMG), spherical micelles appeared to be the dominant population, accompanied by a significantly smaller population of worm-like structures. Finally, in the complete absence of the nitrogen heteroatom, as in the case of PEG-*b*-PBG, the micelles exhibited a spherical morphology. The general size trends observed from TEM were reasonably consistent with the trends in D_h estimated from DLS (**Table 2**). For the PEG-*b*-PMG micelles, it also suggested that the shape of the micelles was strongly influenced by the pyridine regioisomer when prepared by film hydration.

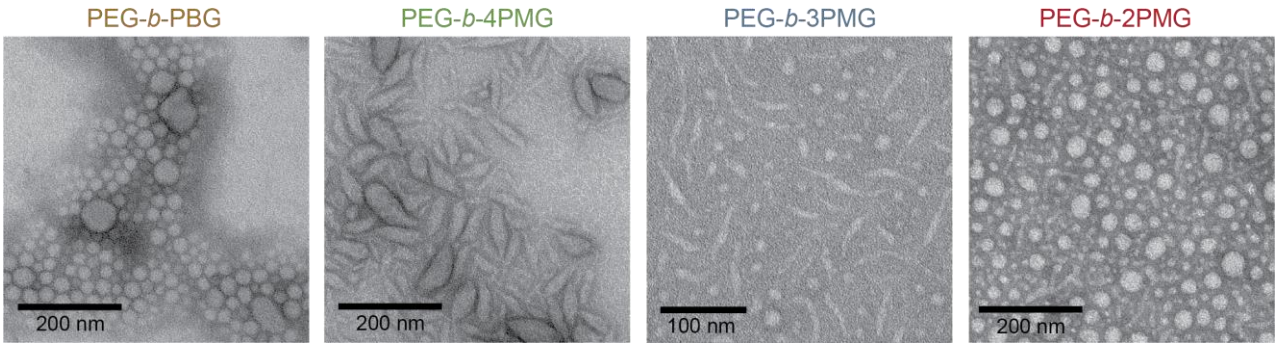


Figure 3. TEM micrographs of PEG-*b*-PBG and PEG-*b*-PMG micelles prepared in 154 mM KCl at pH 7.4. Samples were negatively stained using 2% w/v uranyl acetate.

Nevertheless, it cannot be excluded that a change to morphology may have occurred during the processing of samples for TEM, where the drying/wicking process may have resulted in distortion of the micelle shape. As a result, the TEM images may not have necessarily been

reflective of the micelles as they exist in solution. Therefore, to corroborate the TEM and DLS findings, SAXS was performed on the micelles to gain better insight into their morphology in solution.

SAXS analysis of the PEG-*b*-PBG and PEG-*b*-PMG micelles was initially conducted at various polymer and salt concentrations to identify the optimal conditions to maximise the signal-to-noise ratio from the micelles, while minimising significant secondary aggregation (SI, **Figure S10**). Ultimately, concentrations of 0.5 or 1 mg/mL were employed, respectively, at a salt concentration of 154 mM KCl. Guinier analysis of the scattering profiles was initially performed to calculate the radius of gyration (R_g) (**Table 2**). Unfortunately, this analysis could not be performed on the PEG-*b*-4PMG micelles, since no Guinier plateau could be observed for this polymer.

Subsequently, pair distance distribution functions (i.e., p(r) functions) were generated by indirect Fourier transformation of the SAXS data to provide qualitative information on the size and shape of the aggregates in solution, since different particle shapes give rise to distinct profile shapes in a p(r) function.[50, 51] The p(r) functions also served to identify the maximum particle dimension, D_{max}, and provide insight into appropriate models to use in subsequent form factor modelling.[52] The p(r) functions for the PEG-*b*-PBG, PEG-*b*-3PMG and PEG-*b*-2PMG micelles (**Figure 4**) displayed approximately gaussian distributions; however, slight extended tailing was observed at high values of *r*, which suggested that the particles possessed an elongated dimension (such as in the case of ellipsoids, rods, or cylinders).[50] Additionally, the peak maximum at a lower value of *r* observed in the p(r) function of the PEG-*b*-3PMG micelles indicated that they formed narrower particles, supporting the worm-like morphology observed in the TEM micrographs. The D_{max} values for the PEG-*b*-PBG, PEG-*b*-3PMG and PEG-*b*-2PMG micelles were ~ 600 Å, which

is within the expected size range based on previous analyses by DLS and TEM. Meanwhile, the shape of the p(r) function for PEG-*b*-4PMG appeared to be more akin to an elongated disc, with a significantly higher D_{max} value at ~ 1000 Å. These general size trends supported those observed by DLS and TEM, which suggested that the PEG-*b*-4PMG micelles were the largest out all polymers investigated. However, it should be noted that it is not possible to accurately determine the true D_{max} value for the PEG-*b*-4PMG micelles as the *q* range used in these analyses was not sufficiently low enough in *q* to observe the Guinier plateau.

The SAXS profiles were then fitted to theoretical models of various form factors to further elucidate the size and shape of the micelles in solution at pH 7.4 (**Figure 4**). The X-ray scattering length densities (SLDs) used for modelling were obtained from previously reported literature values ($SLD_{PEG} = 9.30 \times 10^{-6}$ Å^{-2} and $SLD_{water} = 9.47 \times 10^{-6}$ Å^{-2}),[13, 53] with a low scattering contrast between the shell and the solvent expected due to hydration of the PEG corona (i.e., $SLD_{shell} \approx SLD_{solvent}$). Scattering from the core was therefore thought to dominate the scattered X-ray intensity, with the PEG corona only providing a weak contribution to the scattering pattern.[53] The theoretical SLD_{PMG} and SLD_{PBG} were estimated to be 11.2×10^{-6} Å^{-2}, based on the predicted mass density of the *γ*-benzyl-L-glutamate monomer and the molecular formulae of the respective monomeric units.[13]

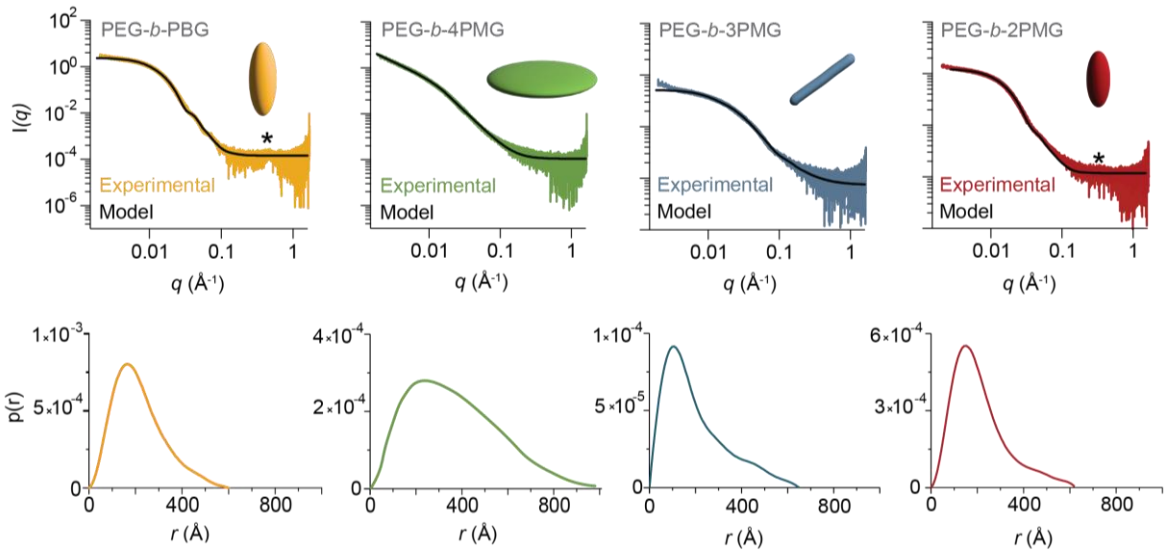


Figure 4. SAXS profiles and fitted theoretical form factor models (top) and p(r) functions (bottom) of PEG-*b*-PBG (core_shell_ellipsoid), PEG-*b*-4PMG (Guinier Porod), PEG-*b*-3PMG (core_shell_cylinder + mono_gauss_coil) and PEG-*b*-2PMG (core_shell_ellipsoid) micelles. Insets illustrate the morphology of the micelles. * Refers to diffraction peak at $q \approx 0.45$ Å^{-1} arising from α-helical domains.

Given the apparent spherical appearance of the PEG-*b*-PBG and PEG-*b*-2PMG micelles in the TEM micrographs, form factor modelling of the SAXS profiles was initially attempted using basic spherical models, although these provided suboptimal fits. Therefore, form factor models with a gradually increasing number of parameters were systematically explored (SI, **Table S3**). The scattering profiles were ultimately fitted using a core-shell ellipsoid model, which resulted in the best fit for the data with the lowest number of free parameters (**Figure 4** and SI, **Table S4**).[54, 55] The form factor modelling provided aspect ratios (ρ) of ~ 2.7 and 2.4 (as denoted by the X_core parameter of the model) for the PEG-*b*-PBG and PEG-*b*-2PMG micelles, respectively, indicative of prolate ellipsoids.[54, 55] This was in agreement with the shape of the p(r) functions, which

suggested the presence of particles elongated in one dimension. The core-shell ellipsoid model also allowed for further quantification of these dimensions. For the PEG-*b*-PBG micelles, the equatorial and polar diameters were calculated to be 250 Å and 675 Å, respectively. These values are in good agreement with the peak maxima and D_{max} values obtained from the p(r) functions, which suggests that the p(r) functions are only representative of the micelle core. Again, this may be explained by the weak scattering of the well-hydrated PEG corona. The shell was calculated to be thicker at the polar ends of the ellipsoid (161 Å) compared to equatorially (47 Å). The PEG-*b*-2PMG micelles were, on average, slightly smaller than their PEG-*b*-PBG counterparts, with equatorial and polar diameters of 210 and 513 Å, respectively, which may be related to the shorter average molecular weight of the core-forming block. The thickness of the shell was calculated to be 62 Å at the polar ends, and 31 Å equatorially.

Form factor modelling of the SAXS profiles for PEG-*b*-4PMG revealed an optimal fit to the Guinier-Porod model (SI, **Table S4**).[56] This model contains a dimension variable (*s*), the value of which is characteristic of different shapes; for spheres $s = 0$, for rods $s = 1$, and for platelets/discs $s = 2$.[56] For the PEG-*b*-4PMG micelles, $s = 1.4$, indicating that the particles were an intermediate shape between a rod and platelet in solution (i.e., flat and elongated). This supports the findings from TEM, which depicted elongated, disc-like particles.

Supported by the presence of a population of elongated/worm-like particles in the TEM micrographs, the PEG-*b*-3PMG micelle SAXS profile was best fitted using a core-shell cylinder form factor model in the low q region in combination with a monodisperse gaussian coil form factor to model the q^{-2} power law observed at high q (SI, **Tables S4–5**). The length and radius of the cylinders was calculated to be 653 and 92 Å, respectively, which supports the D_{max} observed in the corresponding SAXS p(r) function. Modelling the scattering contribution of the polymer

chains at high q using the monodisperse gaussian coil form factor provided a R_g of 40 Å, analogous to that for the polymers in their unimeric state (i.e., when prepared by dissolution of the polymer in aqueous solution at pH 2.5; SI, **Table S6**). Together, these findings are consistent with the presence of a population of cylindrical particles and free polymer.

Overall, form factor modelling of the SAXS profiles of the PEG-*b*-PMG micelles provided further indication that micelle morphology is influenced by the position of the pendant pyridine heteroatom, with micelle shapes ranging from ellipsoids to cylinders to discs when prepared by film hydration. However, it is also worth noting that, for the PEG-*b*-PMG micelles, these observed morphologies may represent metastable aggregates influenced by the choice of self-assembly method and may not necessarily reflect the most thermodynamically stable morphology (*vide infra*).

Aside from providing insight into the micelle shape, the SAXS profiles also revealed the presence of a broad diffraction peak at high q for the PEG-*b*-PBG and PEG-*b*-2PMG micelles ($q \approx 0.45$ Å^{-1}), corresponding to a d-spacing ($2\pi/q$) of ~ 1.3 nm. This has previously been reported to arise due to hexagonal arrays generated by α-helical domains.[13] While this peak was subtle for the PEG-*b*-2PMG micelles, it was noticeably absent for the PEG-*b*-3PMG and PEG-*b*-4PMG micelles, potentially suggesting the absence of α-helical conformations. PEG-*b*-PBG has been extensively reported to form α-helical secondary structures at neutral pH as a result of H-bonding along the polypeptide backbone.[57] The PEG-*b*-PMG copolymers, therefore, were also thought to possess the ability to exhibit these higher order structures due to their structural similarity to PEG-*b*-PBG. Hence, with an emerging view of the relationship between regioisomers and micelle morphology, it was hypothesised that the differences in micelle size and shape may be associated

with changes to the secondary structure of the polypeptide block, directed by the specific regioisomers.

Characterisation of polypeptide secondary structure in micelles

To investigate whether the differences in micelle morphology could be explained by changes in secondary structure, CD spectroscopy was performed on the micelles to better understand their conformation in solution (**Figure 5**). It is important to mention that the base-catalysed deprotection strategy used during the synthesis of these materials has previously been associated with racemisation of the polypeptide backbone,[58] which could influence the resulting secondary structures. Therefore, CD spectroscopy was performed on the PEG-*b*-PGA precursor to explore the extent of racemisation following deprotection and provide a profile for which the secondary structures of the PEG-*b*-PMGs could be compared (SI, **Figure S11**). This revealed that the PEG-*b*-PGA exhibited two minima at ~ 203 and 222 nm in the CD profile. Compared to a typical α-helical CD spectrum, there was a distinct blue-shift from 208 to 203 nm, as well as a reduction in the intensity of the band at 222 nm. This coincided with a reduction in the signal intensity. Together, these findings suggest that the PEG-*b*-PGA adopts an α-helical secondary structure, but with an increased proportion of random coils, indicating that some racemisation may have occurred. It is possible that this racemisation may contribute to the observed secondary structures and, in turn, the micelle morphology.[13] In any case, all PEG-*b*-PMGs were synthesised from the same PEG-*b*-PGA precursor material, and therefore the effect of adding different regioisomers on the secondary structure could still be qualitatively compared (**Figure 5**).

The CD spectra of the PEG-*b*-PBG and PEG-*b*-2PMG micelles were dominated by α-helical secondary structures, as evidenced by the characteristic double minima at ~ 208 and 222 nm, and maxima at approximately ~ 195 nm. This supported the SAXS data, for which diffraction peaks were observed for these two micelles attributed to α-helical domains. Interestingly, the ratios of the bands at 208 and 222 nm were atypical for α-helices, with a significantly greater amplitude

at 222 nm. However, this may be explained by aggregation, as previously reported for micelles containing polypeptide blocks.[59, 60] For example, the band at 222 nm corresponds to the $n-\pi^*$ transition of the polypeptide carbonyl group, and is influenced by intra- and intermolecular interactions.[59] Aggregation can result in changes to the local environment, manifesting as changes to the position and intensity of the peak.[59] In contrast, the PEG-*b*-3PMG and PEG-*b*-4PMG polymers appeared to exhibit a more β-sheet like secondary structure, marked by the single minimum observed in the CD spectra at ~ 218–221 nm. These CD profiles were distinctly different from that observed for the PEG-*b*-PGA precursor, and suggests that the position of the pyridyl nitrogen atom influences the secondary structure of the polypeptides. This may, in turn, influence the self-assembly and morphology of the resulting micelles.

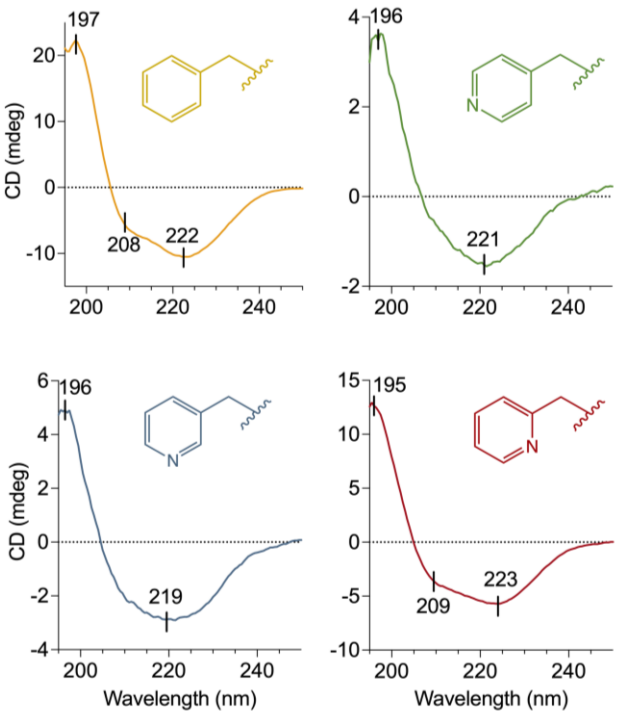


Figure 5. CD spectra of the PEG-*b*-PBG and PEG-*b*-PMG copolymer micelles.

To corroborate the findings from CD spectroscopy, the secondary structure of the polypeptide backbone was further probed *via* ATR-FTIR spectroscopy of the lyophilised micelles (**Figure 6**). While the drying process, in theory, has the potential to alter H-bonding, lyophilisation was thought to better preserve the secondary structure of the polypeptides compared to other approaches that require heating to remove the solvent. The transmittance spectra revealed that all copolymers exhibited an amide I band at 1651–1657 cm^{-1} and amide II band at 1548 cm^{-1} typical of α-helical secondary structures. The amide I band of the PEG-*b*-PBG micelles appeared at a slightly lower wavenumber compared to the PEG-*b*-PMG polymers, likely due to a difference in the orientation of the C=O and N–H groups, leading to a shorter hydrogen bond length between these groups, increased hydrogen bond strength and, as a result, a lower C=O stretching frequency.[61] Amide bands corresponding to inter-/intra-molecular β-sheet conformations were observed for the PEG-*b*-4PMG, PEG-*b*-3PMG and PEG-*b*-PBG micelles, marked by a signal at ~ 1625 cm^{-1}. Additional peaks were observed at 1605 cm^{-1} for PEG-*b*-4PMG micelles and 1577 cm^{-1} for PEG-*b*-3PMG micelles, which may represent intermolecular β-strand and β-turn interactions, respectively.[29] These findings suggest that the micelles contain a mixture of α-helical and β-sheet secondary structures.

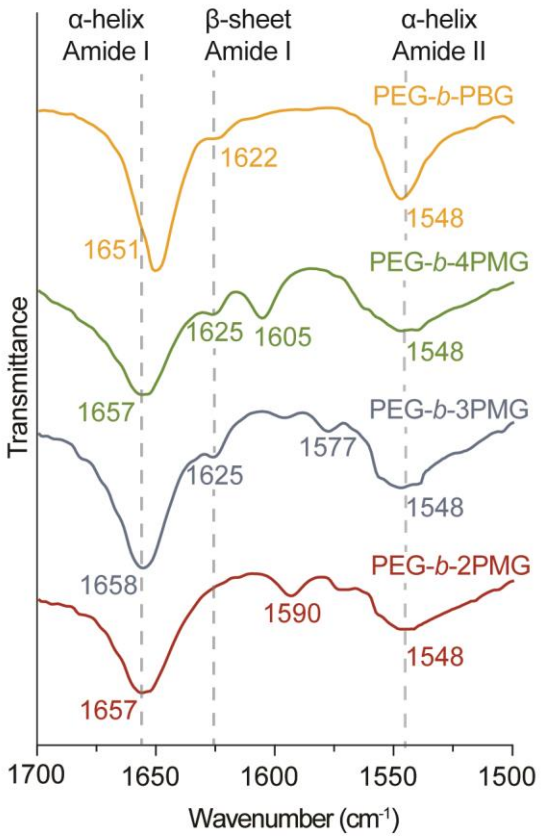


Figure 6. Stacked ATR-FTIR spectra of micellised and lyophilised PEG-*b*-PBG and PEG-*b*-PMG copolymers.

To quantify the proportion of each secondary structure present in the micelles, deconvolution of the amide I peak was performed using second derivative analysis of the spectral data (**Figure 7**). The minima in the second derivative spectra correspond to the presence of local maxima in the original absorbance spectra, allowing for the individual bands to be resolved.[62] It is worth noting, however, that this method can deteriorate the signal-to-noise ratio, and therefore, the absorbance data was smoothed using a 4-point Savitzky-Golay function prior to analysis in order to reduce noise. Curve fitting was performed using the Voigt function, and peaks assigned to specific secondary structures based on their characteristic frequencies and assignments from the

literature.[29, 61] The percentages of each secondary structure were then quantified using the area of each peak relative to the total area of the deconvoluted peaks in the amide I region (**Table 3**).

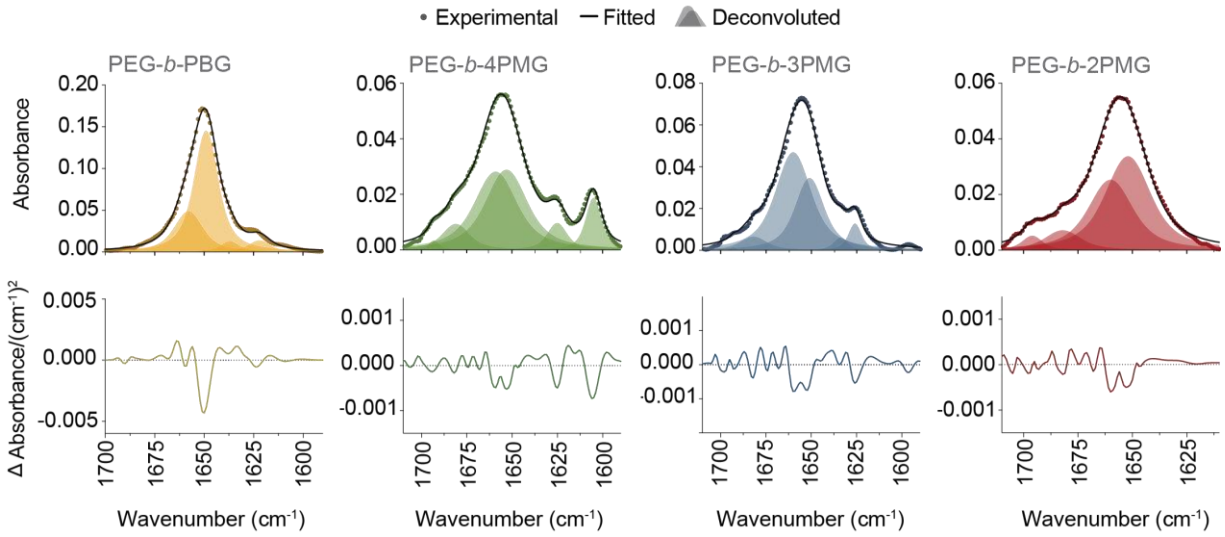


Figure 7. Deconvolution of the amide I peak in the ATR-FTIR absorbance spectra (top) and second derivative of the absorbance data (bottom), whereby peak minima correspond to peak maxima in the original spectra of the lyophilised micelles.

Table 3. Percentages of each secondary structure in PEG-*b*-PBG and PEG-*b*-PMG copolymer micelles as calculated by deconvolution of the FTIR amide I band.

Secondary structure assignments (%)	Polymer			
	PEG-*b*-PBG	PEG-*b*-4PMG	PEG-*b*-3PMG	PEG-*b*-2PMG
Intermolecular β-sheet	5	15	6	0
β-sheet	4	0	2	0
α-helix	91	38	32	88
β-turn	0	47	60	12

Based on deconvolution of the FTIR data, the PEG-*b*-PBG and PEG-*b*-2PMG copolymers exhibited the highest proportions of α-helices, with a small contribution from β-sheets or β-turns,

respectively. Contrastingly, the residues of PEG-*b*-4PMG and PEG-*b*-3PMG predominantly form β-turns, with a contribution of α-helices and β-sheets. These results generally support the findings from CD and SAXS analysis, suggesting that the pyridine regioisomers may play a role in dictating the structural ordering of the polypeptide in the micelle core and the proportions of each secondary structure in the polymer. This indicates that the pyridine nitrogen may have the ability to form stabilising/destabilising hydrogen bonding interactions (both intra- and intermolecularly), depending on where it is located in the pyridine ring. In an attempt to investigate this, the aromatic C=N stretches of the pyridine groups of the polymer were investigated by FTIR spectroscopy and compared to complementary monomeric pyridine derivatives (**Figure S12**), which could, in theory, show changes to the frequency of the C=N stretch depending on changes in H-bonding. Unfortunately, overlap of these stretches with the polypeptide amide II bands made it difficult to conclusively support this theory. In a previous study, Ernst *et al.* prepared a trispyridylamide scaffold as an α-helix foldamer mimetic, where stabilising hydrogen-bonds between the amide moieties and pyridine nitrogens generated stable helical conformations.[63] It is within reason, therefore, that the changing positions of the heteroatom in the pyridine regioisomers of the PMG block may be able to orient in different ways, either promoting or disfavouring certain secondary structures, although further studies are required to investigate this hypothesis. Since the intra- and intermolecular interactions of the polymer chains can govern the self-assembly behaviour of amphiphilic copolymers, differences in secondary structure are likely to influence the overall morphology of the micelles due to differences in core packing.[64] Overall, our findings suggest that the position of the pyridine heteroatom in the pendant groups of PEG-*b*-PMG regioisomers can influence the dominant secondary structures of the copolymer micelles in solution. As a result,

these differences in secondary structure may contribute to changes in micelle morphology after self-assembly.

Thermodynamic and kinetic considerations

While these changes in secondary structure appear to be associated with changes to micelle morphology, it is important to consider the other factors that are also likely to significantly contribute to the observed results. For example, the PEG-*b*-PMG copolymer micelles were prepared by a film hydration approach, which is largely under kinetic control due to the poor solvent quality of the aqueous phase for the core-forming block. This could hinder migration of polymer chains into their most thermodynamically stable state and effectively trap the micelles in kinetically 'frozen' morphologies.[65, 66] Contrastingly, the film hydration approach could not be used for the PEG-*b*-PBG micelles due to extensive precipitation of the polymer because of its higher hydrophobicity. The PEG-*b*-PBG micelles were therefore prepared by an alternative method, solvent evaporation, to promote self-assembly. However, this technique is under greater thermodynamic control, meaning the observed morphologies of the PEG-*b*-PBG micelles are likely to represent a more thermodynamically stable morphology. As a result, a direct comparison between the PEG-*b*-PBG and PEG-*b*-PMG micelles may not be possible due to confounding factors, other than secondary structure, which contribute to the observed morphology. Comparison of the PEG-*b*-PMGs, which were all prepared using the same self-assembly method, reveal interesting changes in morphology observed for different PEG-*b*-PMG regioisomers, though these may represent metastable aggregates. The influence of different self-assembly techniques on the morphology of these PEG-*b*-PMG micelles is the subject of ongoing work within our group.

Conclusions

A series of PEG-*b*-homopolypeptide copolymers were prepared by ROP of a benzyl-L-glutamate NCA and subsequent base-catalysed deprotection, generating the PEG-*b*-PGA precursor. Through a carbodiimide coupling strategy, the pendant carboxylic acid groups of PEG-

b-PGA were then furnished with three different pyridine derivatives (*para*, *meta*, and *ortho*-(hydroxymethyl)pyridine) *via* ester linkages to generate a small library of PEG-*b*-PMG regioisomers. A structural analogue of the copolymer, PEG-*b*-PBG, was also prepared, which possessed a benzyl group in place of the pyridyl moiety. DLS, TEM, and SAXS revealed that the choice of pyridyl regioisomer influenced the size and shape of the copolymer micelles in aqueous solutions at pH 7.4 when prepared by film hydration. PEG-*b*-PBG and PEG-*b*-2PMG formed ellipsoidal micelles in solution, PEG-*b*-3PMG displayed predominantly cylindrical/worm-like micelles, while PEG-*b*-4PMG formed micelles with an intermediate shape between a rod and a disc. This diversity in micelle shape was thought to be related to differences in secondary structure of the polypeptide block, where PEG-*b*-2PMG and PEG-*b*-PBG micelles exhibited predominantly α-helical secondary structures, while β-turn conformations were dominant for PEG-*b*-3PMG and PEG-*b*-4PMG micelles. These results suggest that the position of the pyridine heteroatom may contribute to stabilising/destabilising interactions that play a role in controlling secondary structure, core packing, and subsequent micelle morphology. However, it is important to note that the choice of self-assembly methods used in this study may have contributed to the observed PEG-*b*-PBG and PEG-*b*-PMG micelle morphologies, and therefore, interrogation of the relationship between micellisation technique and morphology is the subject of ongoing work. Overall, this study provides unique insights into how subtle changes in molecular architecture can impact secondary conformation, and in turn, micelle morphology. This nuanced understanding of structure-property relationships enhances our ability to tailor nanoparticles for specific biomedical applications and offers practical insights for the rational design of nanocarriers for drug delivery.

ASSOCIATED CONTENT

Supporting information

^{13}C spectrum of γ-benzyl-L-glutamate NCA (Figure S1); ^{1}H NMR spectrum of supernatant from synthesis of PEG-*b*-PBG copolymer by ROP (Figure S2); GPC chromatograms of PEG-NH_2 and PEG-*b*-PBG (Figure S3); optimisation of reaction conditions for carbodiimide coupling reaction (Table S1); thermal characterisation of copolymers, including TGA (Figure S4) and DSC thermograms (Figure S5), and a summary of copolymer thermal properties (Table S2); CMC determination, including pyrene fluorescence spectra and fluorescence emission ratio plotted against polymer concentration (Figure S6); ^{1}H NMR spectra of micelles in D_2O (neutral pH, Figure S7); DLS PSDs (number, volume, intensity) of micelles (Figure S8); TEM number distributions of micelles (Figure S9); optimisation of SAXS experimental parameters, including polymer and salt concentration (Figure S10); SAXS form factor modelling of micelles using basic spherical and ellipsoid models (Table S3); optimised SAXS form factor modelling of micelles (Table S4); individual contributions of models for SAXS form factor modelling of PEG-*b*-3PMG (Table S5); SAXS form factor modelling of PEG-*b*-3PMG at pH 2.5 using monodisperse gaussian coil model (Table S6); CD spectrum of PEG-*b*-PGA (Figure S11); ATR-FTIR spectra of PEG-*b*-PMG copolymers and model compounds (Figure S12).

Acknowledgements

This research was undertaken on the SAXS/WAXS beamline at the Australian Synchrotron, part of ANSTO (18917/21015). The authors acknowledge the instruments and expertise of Microscopy Australia at Adelaide Microscopy, The University of Adelaide, enabled by NCRIS, university, and state government support. The authors would also like to acknowledge Professor David Beattie from the University of South Australia for the fruitful discussion and expertise relating to deconvolution of the FTIR data. The authors thank the Royal Australian Chemical Institute (RACI) Polymer Division, Dr Ian Gould AM, American Chemical Society CAS Future Leaders Program, and Soroptimist International of Adelaide Inc. for their generous financial support.

AUTHOR INFORMATION

Corresponding Author

* Anton Blencowe – Applied Chemistry and Translational Biomaterials (ACTB) Group, Centre for Pharmaceutical Innovation (CPI), UniSA Clinical and Health Sciences, University of South Australia, Adelaide SA 5001, Australia; orcid.org/0000-0002-7630-4874; Email: anton.blencowe@unisa.edu.au

Author Contributions

The manuscript was written through contributions of all authors. Project conceptualisation was performed by A.B., C.D., T.A.G., H.A., and M.K.H. Supervision was performed by A.B., A.J.C., T.A.G., H.A., and M.K.H. Funding acquisition was performed by A.B. and C.D. Methodology, investigation and formal analysis were completed by C.D. and A.B. A.J.C. contributed to methodology, investigation, and formal analysis of SAXS studies. C.D. wrote the original draft. A.B., A.J.C., T.A.G., H.A., and M.K.H. reviewed and edited the manuscript.

Funding Sources

This research was supported by an AINSE Ltd. Postgraduate Research Award (PGRA). The work was also funded by an Australian Government Research Training Program (RTP) Scholarship and Gould Experimental Science Grant Commendation Award. Todd Gillam is the recipient of an Office of National Intelligence National Intelligence Postdoctoral Grant (project number NIPG-2022-001) funded by the Australian Government.

Notes

The authors declare no competing financial interest.

References

1. Dharmayanti, C.; Gillam, T. A.; Klingler-Hoffmann, M.; Albrecht, H.; Blencowe, A., Strategies for the development of ph-responsive synthetic polypeptides and polymer-peptide hybrids: recent advancements. *Polymers* **2021**, *13*, 624.

2. Bonduelle, C., Secondary structures of synthetic polypeptide polymers. *Polym. Chem.* **2018**, *9* (13), 1517–1529.

3. Maier, M.; Kotman, N.; Friedrichs, C.; Andrieu, J.; Wagner, M.; Graf, R.; Strauss, W. S. L.; Mailänder, V.; Weiss, C. K.; Landfester, K., Highly site specific, protease cleavable, hydrophobic peptide–polymer nanoparticles. *Macromolecules* **2011**, *44* (16), 6258–6267.

4. Standley, S. M.; Toft, D. J.; Cheng, H.; Soukasene, S.; Chen, J.; Raja, S. M.; Band, V.; Band, H.; Cryns, V. L.; Stupp, S. I., Induction of cancer cell death by self-assembling nanostructures incorporating a cytotoxic peptide. *Cancer Res.* **2010**, *70* (8), 3020–3026.

5. Song, Z.; Tan, Z.; Cheng, J., Recent advances and future perspectives of synthetic polypeptides from *N*-carboxyanhydrides. *Macromolecules* **2019**, *52* (22), 8521–8539.

6. Matsumura, Y., Preclinical and clinical studies of NK012, an SN-38-incorporating polymeric micelles, which is designed based on EPR effect. *Adv. Drug Deliv. Rev.* **2011**, *63* (3), 184–192.

7. Arroyo-Crespo, J. J.; Armiñán, A.; Charbonnier, D.; Balzano-Nogueira, L.; Huertas-López, F.; Martí, C.; Tarazona, S.; Forteza, J.; Conesa, A.; Vicent, M. J., Tumor microenvironment-targeted poly-L-glutamic acid-based combination conjugate for enhanced triple negative breast cancer treatment. *Biomaterials* **2018**, *186*, 8–21.

8. Barbosa, M. E. M.; Montembault, V.; Cammas-Marion, S.; Ponchel, G.; Fontaine, L., Synthesis and characterization of novel poly(γ-benzyl-L-glutamate) derivatives tailored for the preparation of nanoparticles of pharmaceutical interest. *Polym. Int.* **2007**, *56* (3), 317–324.

9. Tang, H.; Zhang, D., General route toward side-chain-functionalized α-helical polypeptides. *Biomacromolecules* **2010**, *11* (6), 1585–1592.

10. Mochida, Y.; Cabral, H.; Miura, Y.; Albertini, F.; Fukushima, S.; Osada, K.; Nishiyama, N.; Kataoka, K., Bundled assembly of helical nanostructures in polymeric micelles loaded with platinum drugs enhancing therapeutic efficiency against pancreatic tumor. *ACS Nano* **2014**, *8* (7), 6724–6738.

11. Zhuang, Z.; Cai, C.; Jiang, T.; Lin, J.; Yang, C., Self-assembly behavior of rod–coil–rod polypeptide block copolymers. *Polymer* **2014**, *55* (2), 602–610.

12. Shen, J.; Chen, C.; Fu, W.; Shi, L.; Li, Z., Conformation-specific self-assembly of thermo-responsive poly(ethylene glycol)-b-polypeptide diblock copolymer. *Langmuir* **2013**, *29* (21), 6271–6278.

13. Grazon, C.; Salas-Ambrosio, P.; Antoine, S.; Ibarboure, E.; Sandre, O.; Clulow, A. J.; Boyd, B. J.; Grinstaff, M. W.; Lecommandoux, S.; Bonduelle, C., Aqueous ROPISA of α-amino acid N-carboxyanhydrides: polypeptide block secondary structure controls nanoparticle shape anisotropy. *Polym. Chem.* **2021**, *12* (43), 6242–6251.

14. Chécot, F.; Brûlet, A.; Oberdisse, J.; Gnanou, Y.; Mondain-Monval, O.; Lecommandoux, S., Structure of polypeptide-based diblock copolymers in solution: stimuli-responsive vesicles and micelles. *Langmuir* **2005**, *21* (10), 4308–4315.

15. Kramer, J. R.; Rodriguez, A. R.; Choe, U.-J.; Kamei, D. T.; Deming, T. J., Glycopolypeptide conformations in bioactive block copolymer assemblies influence their nanoscale morphology. *Soft Matter* **2013**, *9* (12), 3389–3395.

16. Li, T.; Lin, J.; Chen, T.; Zhang, S., Polymeric micelles formed by polypeptide graft copolymer and its mixtures with polypeptide block copolymer. *Polymer* **2006**, *47* (13), 4485–4489.

17. Deming, T. J., Synthesis of side-chain modified polypeptides. *Chem. Rev.* **2016**, *116* (3), 786–808.

18. Brewer, K.; Bai, F.; Blencowe, A. pH-Responsive poly(ethylene glycol)-b-poly(2-vinylpyridine) micelles for the triggered release of therapeutics *Pharmaceutics* **2023**, *15* (3), 977.

19. Mishra, A. K.; Lim, J.; Lee, J.; Park, S.; Seo, Y.; Hwang, H.; Kim, J. K., Control drug release behavior by highly stable and pH sensitive poly(N-vinylpyrrolidone)-block-poly(4-vinylpyridine) copolymer micelles. *Polymer* **2021**, *213*, 123329.

20. Park, E. S.; Kim, H. S.; Kim, M. N.; Yoon, J. S., Antibacterial activities of polystyrene-block-poly(4-vinyl pyridine) and poly(styrene-random-4-vinyl pyridine). *Eur. Polym. J.* **2004**, *40* (12), 2819–2822.

21. Tiller, J. C.; Lee, S. B.; Lewis, K.; Klibanov, A. M., Polymer surfaces derivatized with poly(vinyl-N-hexylpyridinium) kill airborne and waterborne bacteria. *Biotechnol. Bioeng.* **2002**, *79* (4), 465–471.

22. Salatin, S.; Maleki Dizaj, S.; Yari Khosroushahi, A., Effect the surface modification, size, and shape on cellular uptake of nanoparticles. *Cell Bio. Int.* **2015**, *39* (8), 881–890.

23. Yu, Q.; Roberts, M. G.; Houdaihed, L.; Liu, Y.; Ho, K.; Walker, G.; Allen, C.; Reilly, R. M.; Manners, I.; Winnik, M. A., Investigating the influence of block copolymer micelle length on cellular uptake and penetration in a multicellular tumor spheroid model. *Nanoscale* **2021**, *13* (1), 280–291.

24. Dzuricky, M.; Xiong, S.; Weber, P.; Chilkoti, A., Avidity and cell uptake of integrin-targeting polypeptide micelles is strongly shape-dependent. *Nano Lett.* **2019**, *19* (9), 6124–6132.

25. Fulmer, G. R.; Miller, A. J. M.; Sherden, N. H.; Gottlieb, H. E.; Nudelman, A.; Stoltz, B. M.; Bercaw, J. E.; Goldberg, K. I., NMR chemical shifts of trace impurities: common laboratory solvents, organics, and gases in deuterated solvents relevant to the organometallic chemist. *Organometallics* **2010,** *29* (9), 2176-2179.

26. Schneider, C. A.; Rasband, W. S.; Eliceiri, K. W., NIH Image to ImageJ: 25 years of image analysis. *Nat. Methods* **2012**, *9* (7), 671–675.

27. Kirby, N. M.; Mudie, S. T.; Hawley, A. M.; Cookson, D. J.; Mertens, H. D. T.; Cowieson, N.; Samardzic-Boban, V., A low-background-intensity focusing small-angle X-ray scattering undulator beamline. *J. Appl. Crystallogr.* **2013**, *46* (6), 1670–1680.

28. Wojdyr, M., Fityk: a general-purpose peak fitting program. *J. Appl. Crystallogr.* **2010**, *43* (5), 1126–1128.

29. Kong, J.; Yu, S., Fourier transform infrared spectroscopic analysis of protein secondary structures. *Acta Biochim. Biophys. Sin.* **2007**, *39* (8), 549–559.

30. Daly, W. H.; Poché, D., The preparation of N-carboxyanhydrides of α-amino acids using bis(trichloromethyl)carbonate. *Tetrahedron Lett.* **1988**, *29* (46), 5859–5862.

31. Kalyanasundaram, K.; Thomas, J. K., Environmental effects on vibronic band intensities in pyrene monomer fluorescence and their application in studies of micellar systems. *J. Am. Chem. Soc.* **1977**, *99* (7), 2039–2044.

32. Hussain, M. S.; Faisal, K. S.; Clulow, A. J.; Albrecht, H.; Krasowska, M.; Blencowe, A. Influence of lyophilization and cryoprotection on the stability and morphology of drug-loaded poly(ethylene glycol-b-epsilon-caprolactone) micelles. *Polymers* **2023**, *15* (8), 1974.

33. Saddam Hussain, M.; Khetan, R.; Clulow, A. J.; Ganesan, R.; MacMillan, A.; Robinson, N.; Ahmed-Cox, A.; Krasowska, M.; Albrecht, H.; Blencowe, A., Teaching an old dog new tricks: a global approach to enhancing the cytotoxicity of drug-loaded, non-responsive micelles using oligoelectrolytes. *ACS Appl. Mater. Interfaces* **2024**, *6* (8), 9736–9748.

34. Guo, J.; Huang, Y.; Jing, X.; Chen, X., Synthesis and characterization of functional poly(γ-benzyl-L-glutamate) (PBLG) as a hydrophobic precursor. *Polymer* **2009**, *50* (13), 2847–2855.

35. Habraken, G. J. M.; Peeters, M.; Dietz, C. H. J. T.; Koning, C. E.; Heise, A., How controlled and versatile is N-carboxy anhydride (NCA) polymerization at 0 °C? Effect of temperature on homo-, block- and graft (co)polymerization. *Polym. Chem.* **2010**, *1* (4), 514–524.

36. Wibowo, S. H.; Wong, E. H. H.; Sulistio, A.; Guntari, S. N.; Blencowe, A.; Caruso, F.; Qiao, G. G., Assembly of free-standing polypeptide films via the synergistic combination of hyperbranched macroinitiators, the grafting-from approach, and cross-chain termination. *Adv. Mater.* **2013**, *25* (33), 4619–4624.

37. Vayaboury, W.; Giani, O.; Cottet, H.; Deratani, A.; Schué, F., Living polymerization of α-amino acid N-carboxyanhydrides (NCA) upon decreasing the reaction temperature. *Macromol. Rapid Commun.* **2004**, *25* (13), 1221–1224.

38. Nalbone, J. M.; Lahankar, N.; Buissereth, L.; Raj, M., Glutamic acid selective chemical cleavage of peptide bonds. *Org. Lett.* **2016**, *18* (5), 1186–1189.

39. Chen, L.; Ci, T.; Li, T.; Yu, L.; Ding, J., Effects of molecular weight distribution of amphiphilic block copolymers on their solubility, micellization, and temperature-induced sol–gel transition in water. *Macromolecules* **2014**, *47* (17), 5895–5903.

40. Huesmann, D.; Birke, A.; Klinker, K.; Türk, S.; Räder, H. J.; Barz, M., Revisiting secondary structures in NCA polymerization: influences on the analysis of protected polylysines. *Macromolecules* **2014**, *47* (3), 928–936.

41. Lillya, C. P.; Macknight, W. J.; Newman, R. M.; Su, W.-F. A.; Uden, P. C., Thermal degradation of glutamate polymers. *J. Macromol. Sci., Part A: Pure Appl. Chem.* **1980**, *14* (8), 1181–1196.

42. Kojima, T.; Kurotu, T.; Kawaguchi, T., Thermal decomposition of poly(γ-methyl-L-glutamate). *Macromolecules* **1986**, *19* (4), 1281–1284.

43. Kwon, S.-k.; Kim, D., Effect of process parameters of UV-assisted gas-phase cleaning on the removal of PEG (polyethyleneglycol) from a Si substrate. *J. Korean Phys. Soc.* **2014**, 49 *(4)*, 1421–1427.

44. Floudas, G.; Papadopoulos, P.; Klok, H. A.; Vandermeulen, G. W. M.; Rodriguez-Hernandez, J., Hierarchical self-assembly of poly(γ-benzyl-L-glutamate)−poly(ethylene glycol)−poly(γ-benzyl-L-glutamate) rod−coil−rod triblock copolymers. *Macromolecules* **2003**, *36* (10), 3673–3683.

45. Martuscelli, E.; Silvestre, C.; Addonizio, M. L.; Amelino, L., Phase structure and compatibility studies in poly(ethylene oxide)/poly(methyl methacrylate) blends. *Makromol. Chem.* **1986**, *187* (6), 1557–1571.

46. Wan, Q.; Thompson, B. C., Control of properties through hydrogen bonding interactions in conjugated polymers. *Adv. Sci.* **2024**, *11* (8), 2305356.

47. Zhang, J.; Hu, W., Roles of specific hydrogen-bonding interactions in the crystallization kinetics of polymers. *Polymer* **2023**, *283*, 126278.

48. Jeong, Y.-H.; Shin, H.-W.; Kwon, J.-Y.; Lee, S.-M., Cisplatin-encapsulated polymeric nanoparticles with molecular geometry-regulated colloidal properties and controlled drug release. *ACS Appl. Mater. Interfaces* **2018**, *10* (28), 23617–23629.

49. Satoh, M.; Yoda, E.; Hayashi, T.; Komiyama, J., Potentiometric titration of poly (vinylpyridines) and hydrophobic interaction in the counterion binding. *Macromolecules* **1989**, *22* (4), 1808–1812.

50. Dmitri, I. S.; Michel, H. J. K., Small-angle scattering studies of biological macromolecules in solution. *Rep. Prog. Phys.* **2003**, *66* (10), 1735.

51. Glatter, O., A new method for the evaluation of small-angle scattering data. *J. Appl. Crystallogr.* **1977**, *10* (5), 415–421.

52. Kikhney, A. G.; Svergun, D. I., A practical guide to small angle X-ray scattering (SAXS) of flexible and intrinsically disordered proteins. *FEBS Lett.* **2015**, *589* (19, Part A), 2570–2577.

53. Faisal, K. S.; Clulow, A. J.; Krasowska, M.; Gillam, T.; Miklavcic, S. J.; Williamson, N. H.; Blencowe, A., Interrogating the relationship between the microstructure of amphiphilic poly(ethylene glycol-b-caprolactone) copolymers and their colloidal assemblies using non-interfering techniques. *J. Colloid Interface Sci.* **2022**, *606*, 1140–1152.

54. Kotlarchyk, M.; Chen, S. H., Analysis of small angle neutron scattering spectra from polydisperse interacting colloids. *J. Chem. Phys.* **1983**, *79* (5), 2461–2469.

55. Berr, S. S., Solvent isotope effects on alkytrimethylammonium bromide micelles as a function of alkyl chain length. *J. Phys.Chem.* **1987**, *91* (18), 4760–4765.

56. Hammouda, B., A new Guinier–Porod model. *J. Appl. Crystallogr.* **2010**, *43* (4), 716–719.

57. Blout, E. R.; Idelson, M., Polypeptides. VI. Poly-α-L-glutamic acid: preparation and helix-coil conversions. *J. Am. Chem. Soc.* **1956**, *78* (2), 497–498.

58. Hanby, W. E.; Waley, S. G.; Watson, J., Synthetic polyglutamic acid. *Nature* **1948**, *161* (4082), 132–132.

59. Ding, W.; Lin, S.; Lin, J.; Zhang, L., Effect of chain conformational change on micelle structures: experimental studies and molecular dynamics simulations. *J. Phys. Chem. B* **2008**, *112* (3), 776–783.

60. Piedra-Arroni, E.; Makni, F.; Severac, L.; Stigliani, J.-L.; Pratviel, G.; Bonduelle, C. Smart poly(imidazoyl-L-lysine): synthesis and reversible helix-to-coil transition at neutral pH. *Polymers* **2017**, *9* (7), 276.

61. Sadat, A.; Joye, I. J. Peak fitting applied to Fourier transform infrared and raman spectroscopic analysis of proteins. *Appl. Sci.* **2020**, *10* (17), 5918.

62. Dong, A.; Huang, P.; Caughey, W. S., Protein secondary structures in water from second-derivative amide I infrared spectra. *Biochemistry* **1990**, *29* (13), 3303–3308.

63. Ernst, J. T.; Becerril, J.; Park, H. S.; Yin, H.; Hamilton, A. D., Design and Application of an α-helix-mimetic scaffold based on an oligoamide-foldamer strategy: antagonism of the Bak BH3/Bcl-xL complex. *Angew. Chem., Int. Ed.* **2003**, *42* (5), 535–539.

64. Judge, N.; Pavlović, D.; Moldenhauer, E.; Clarke, P.; Brannigan, R.; Heise, A., Influence of the block copolypeptide surfactant structure on the size of polypeptide nanoparticles obtained by mini emulsion polymerisation. *Polym. Chem.* **2022**, *13* (19), 2822–2830.

65. Nicolai, T.; Colombani, O.; Chassenieux, C., Dynamic polymeric micelles versus frozen nanoparticles formed by block copolymers. *Soft Matter* **2010**, *6* (14), 3111–3118.

66. Zhang, L.; Eisenberg, A., Thermodynamic vs kinetic aspects in the formation and morphological transitions of crew-cut aggregates produced by self-assembly of polystyrene-b-poly(acrylic acid) block copolymers in dilute solution. *Macromolecules* **1999**, *32* (7), 2239–2249.

FOR TABLE OF CONTENTS USE ONLY

Table of contents graphic

